Icarus 201 (2009) 634–654

Contents lists available at ScienceDirect

Icarus

www.elsevier.com/locate/icarus

A multilayer model for thermal infrared emission of Saturn's rings: Basic formulation and implications for Earth-based observations

Ryuji Morishima [a,*], Heikki Salo [b], Keiji Ohtsuki [c]

[a] Institute for Theoretical Physics, University of Zurich, Winterthurerstrasse 190, 8057 Zurich, Switzerland
[b] Department of Physical Sciences, Division of Astronomy, P.O. BOX 3000 FIN-90014, University of Oulu, Finland
[c] Laboratory for Atmospheric and Space Physics, University of Colorado, 392 UCB, Boulder, CO 80309-0392, United States

ARTICLE INFO

Article history:
Received 31 July 2007
Revised 24 October 2008
Accepted 24 January 2009
Available online 10 February 2009

Keywords:
Saturn, rings
Infrared observations
Radiative transfer

ABSTRACT

We present our new model for the thermal infrared emission of Saturn's rings based on a multilayer approximation. In our model, (1) the equation of classical radiative transfer is solved directly for both visible and infrared light, (2) the vertical heterogeneity of spin frequencies of ring particles is taken into account, and (3) the heat transport due to particles motion in the vertical and azimuthal directions is taken into account. We adopt a bimodal size distribution, in which rapidly spinning small particles (whose spin periods are shorter than the thermal relaxation time) with large orbital inclinations have spherically symmetric temperatures, whereas non-spinning large particles (conventionally called slow rotators) with small orbital inclinations are heated up only on their illuminated sides. The most important physical parameters, which control ring temperatures, are the albedo in visible light, the fraction of fast rotators ($f_{\rm fast}$) in the optical depth, and the thermal inertia. In the present paper, we apply the model to Earth-based observations. Our model can well reproduce the observed temperature for all the main rings (A, B, and C rings), although we cannot determine exact values of the physical parameters due to degeneracy among them. Nevertheless, the range of the estimated albedo is limited to 0–0.52 ± 0.05, 0.55 ± 0.07–0.74 ± 0.03, and 0.51 ± 0.07–0.74 ± 0.06 for the C, B, and A rings, respectively. These lower and upper limits are obtained assuming all ring particles to be either fast and slow rotators, respectively. For the C ring, at least some fraction of slow rotators is necessary ($f_{\rm fast} \leqslant 0.9$) in order for the fitted albedo to be positive. For the A and B rings, non-zero fraction of fast rotators ($f_{\rm fast} \geqslant 0.1$–$0.2$) is favorable, since the increase of the brightness temperature with increasing solar elevation angle is enhanced with some fraction of fast rotators.

1. Introduction

Saturn's rings have been observed by spacecraft (Pioneer 11, Voyager 1 and 2, and Cassini) and by Earth-based telescopes in the last several decades in various wavelengths from ultraviolet to radio. Although our understanding of the rings has been tremendously improved, the rings are still covered under a lot of mysteries. For example, we do not know their origin, age, and formation mechanism of many of the observed structures. Ring particle properties such as the albedo and size distribution are relatively well determined, although they are still model-dependent. The composition of ring particles is mostly (>90%) H_2O ice (Cuzzi et al., 2002; Poulet et al., 2003), but we do not why it is so dominant.

In order to clarify these problems, the recent observations by Cassini (Porco et al., 2005; Esposito et al., 2005; Flasar et al., 2005) are invaluable. For interpretation of observations, better models are urgently needed. In the modeling of the thermal emission of rings, which we will focus on in the present paper, less progress has been made compared to photometric modeling. The difficulty, which complicates modeling of the thermal emission, is that the thermal response to heat sources (e.g., the Sun), unlike responses in other wavelengths, can not be modeled only with an instantaneous snapshot of a ring, as the thermal energy is transported by the azimuthal, vertical, and spin motion of particles. Therefore, thermal modeling must be directly coupled with dynamics of rings (Cuzzi et al., 1984; Spilker et al., 2003).

The spin frequency of ring particles is a very important factor. If a particle's spin period is much shorter than the thermal relaxation time, the particle radiates the thermal emission over its whole surface area. On the other hand, the thermal emission is mainly from the face illuminated by a heat source if the spin period is long enough. Thus, fast spinning particles are colder than slow rotators when viewed from a direction close to the dominant heat source, as it is the case for Earth-based observations. The heat transport due to the vertical motion of particles is expected to decrease the temperature gradient in the vertical direction, and it is particularly

* Corresponding author. Fax: +41 44 635 5704.
E-mail address: ryuji@physik.uzh.ch (R. Morishima).

0019-1035/$ – see front matter
doi:10.1016/j.icarus.2009.01.019

important for optically thick rings (Cuzzi et al., 1984). Besides the effect of eclipse cooling and subsequent heating (Froidevaux et al., 1981; Ferrari and Leyrat, 2006), the azimuthal motion of particles needs to be taken into account in thermal modeling as the energy flux from Saturn depends on the azimuthal angle.

There are two main types of models used for investigating the thermal response of rings, namely the monolayer model and the multilayer model. The former type of models (Froidevaux, 1981; Ferrari and Leyrat, 2006) explicitly include the effect of finite size of particles, which is important if the particle size is comparable to the mean free path of a photon (i.e., the distance between particles). The intensity due to multiply scattered light is smaller in a monolayer disk as compared with that in a multi-layered ring. The monolayer-like compaction, indeed, can account for many optical photometric properties in the A- and B-rings (Dones et al., 1993; Salo and Karjalainen, 2003). However, the monolayer models are limited to a single layer of uni-sized particles and neglect the contribution from small particles which spread more extensively in the vertical direction.

On the other hand, the multilayer models (Kawata and Irvine, 1975; Kawata, 1983) solve the classical radiative transfer equations (e.g., Chandrasekhar, 1960). Therefore, this type of models are suitable for vertically extended particles layers, but neglect the effects of compaction of particles. Considering the extended size distribution suggested from various observations (Marouf et al., 1983; Zebker et al., 1985; French and Nicholson, 2000), the cross section of vertically extended small particles is significant (see Morishima and Salo, 2006). Even if the fraction of small particles is small, their contribution is expected to become more important as the observer elevation angle, $|B|$, decreases (Salo and Karjalainen, 2003).

Estimations of the ratio of the width to the height of wakes in the A and B rings from Cassini observations (Colwell et al., 2006, 2007; Hedman et al., 2007), combined with the gravitational wake theory (Salo, 1992b, 1995), suggest the thickness of the ring to be of the order of 10 m. This is comparable to the largest particle size (French and Nicholson, 2000). Therefore, the actual rings resemble a monolayer for the largest particles, but are better represented by multilayers for small particles spreading more extensively in the vertical direction.

Dynamical studies support these pictures. They suggest that large particles spinning slowly concentrate near the midplane of the ring whereas small particles spinning rapidly spread more extensively in the vertical direction (Salo, 1987; Richardson, 1994; Ohtsuki, 2005, 2006a, 2006b; Ohtsuki and Toyama, 2005; Morishima and Salo, 2006). It has been also shown that the spin periods of the largest particles are always comparable to the orbital period while the spin period is roughly proportional to the particle size for cases with an extended size distribution.

In order to reflect the ring features obtained from various observations and dynamical studies, we introduce a new thermal model, taking into account the following three effects, which were not included in the previous models appropriately: (1) the equation of classical radiative transfer is solved directly for both visible and infrared light, without any arbitrary approximation concerning the directions of rays, (2) the vertical heterogeneity of spin frequencies of ring particles is taken into account, and (3) the heat transport due to the vertical and azimuthal motion of particles is taken into account. Since we will assume homogeneity in the planar directions, it suffices to solve a one-dimensional radiative transfer equation in the vertical direction. As we solve the equation of classical radiative transfer, we adopt a multilayer approximation, in which the ring thickness is assumed to be much larger than the size of particles. We thus ignore the effects of compaction of particles. The effect needs to be included in future work.

Since most of thermal infrared data for Saturn's rings have been obtained by Earth-based observations, previous models mainly focused on the dependence of the temperature on the solar elevation angle B'. The brightness temperature of Saturn's B ring at ~20 μm increases with the solar elevation angle from 74 K for $|B'| = 6.5°$ to ~95 K for $|B'| \sim 26°$ (see Table 1). The A ring temperature has a similar dependence. We call these rather strong increases of the temperatures the thermal tilt effect (the tilt effect in optical wavelengths is also seen in the B ring but not in the A ring; Esposito and Lumme, 1977). Models based on a monolayer approximation (Froidevaux, 1981; Ferrari and Leyrat, 2006) can apparently well explain the thermal tilt effect for the A and B rings in particular with slowly spinning particles. The monolayer approximation might be appropriate if the total cross section of small particles is negligible and ring particles are very dissipative.

Table 1
Observed brightness temperatures for the A, B, C rings, and Saturn's disk center.[a]

References	$\lvert B'\rvert$ (deg)	$B\frac{B'}{\lvert B'\rvert}$ (deg)	$\alpha_\odot$ (deg)	$a_\odot$ (AU)	λ (μm)	Obs. date	T_b (K)			
							A	B	C	Disk
Morrison (1974)	26.5	26.3	5.4	9.03	20.0	Oct-72, Sep-73		96 ± 3 (95.5)		92 ± 2
Rieke (1975)	26.5	26.0	4.3	9.02	22.5	Nov-73	88.4 ± 1 (86.9)	91.5 ± 1 (90.0)	80.6 ± 1 (79.3)	93.0
Murphy (1973)	26.4	26.4	6.1	9.04	17–25	Aug, Sep-72	89 ± 3 (84.0)	94 ± 2 (88.5)	89 ± 4 (84.0)	97.3 ± 2
Murphy et al. (1972)[b]	24.8			9.07	17–25			93 (87.7)		97.3 ± 2
Leyrat et al. (2008)[c]	21.9	23.0	6.1	9.07	19.5	Apr-05	84 (80.5)	90 (86.0)	85 (81.4)	96
Ferrari et al. (2005)[d]	21.6	20.4	4.2	9.16	20.5	Mar-00	81.0 ± 0.3 (77.3)	89.5 ± 0.3 (85.0)	86.0 ± 0.3 (81.8)	97.0
Ferrari et al. (2005)[d]	19.0	20.9	6.2	9.22	20.5	Jul-99	82.0 ± 0.3 (77.1)	88.5 ± 0.3 (82.8)	86.5 ± 0.3 (81.0)	99.0
Nolt et al. (1978)	16.3	17.8	3.4	9.14	22.7	Mar-77	82.0 (83.5)	84.0 (85.6)	81.0 (82.4)	89.9
Sinton et al. (1980)	16.2	17.9	4.0	9.14	18.1	Mar-77		81 (83.7)	80 (82.6)	88.5
Nolt et al. (1980)	11.8	11	3	9.21	20	Jan-78		77.5 ± 3 (79.3)		89.4
Sinton et al. (1980)	11.5	11.2	1.1	9.22	25	Feb-78		75 (80.3)	78 (83.8)	85
Froidevaux (1981)	10.0	12.8	6.3	9.25	16–26	May-78	75.5 (75.5)	78.6 (78.6)	83.3 (83.3)	92
Nolt et al. (1980)	6.5	4.2	5.1	9.31	20	Jan-79		74 ± 3 (75.9)	85 (87.5)	89.4
Froidevaux et al. (1981)[e]	2.8	2.8		9.24	45 ± 11	Sep-79	62 ± 3 (60.9)			94.4 ± 3
Froidevaux and Ingersoll (1980)[e]	2.8	−1.0		9.24	45 ± 11	Sep-79	54 ± 3 (53.2)			94.4 ± 3
Tokunaga et al. (1980)[f]	0.9	−1.7	5.7	9.42	19.8	Jan-80	56.0 ± 0.9 (56.5)			?

[a] B' is the solar elevation angle, B is the elevation angle of the observer (or the Earth), $\alpha_\odot$ is the solar phase angle, $a_\odot$ is the heliocentric distance, and λ is the wavelength. The temperatures in parentheses are normalized to Saturn's disk center brightness temperature of $T_{\mathrm{disk,st}} = 92$ K at $a_\odot = 9.25$ AU.

[b] Data in Murphy (1973).

[c] T_b's at 80,000, 100,000, and 130,000 km.

[d] Heliocentric distances from the ring node (http://pds-rings.seti.org/).

[e] Pioneer observations.

[f] Disk temperature is unknown and the normalization of the ring temperature is done only for the heliocentric distance.

Kawata (1983) found that the vertically homogeneous multilayers produced a much less steep increase in the temperature with B' than the observed thermal tilt effect for the A and B rings. In order to explain the observed thermal tilt effect, he proposed the vertical heterogeneity of particles' albedo A_V in visible light and particle spins. At small B ($\simeq B'$ for Earth-based observations) an observer mainly sees vertically extended small particles with cold temperatures due to high A_V, whereas large particles concentrated near the disk midplane with warmer temperatures due to smaller A_V start to be visible as B increases. The vertical segregation of large and small particles itself is dynamically reasonable as we mentioned above, and different physical properties with different size of particles might be somewhat probable, such as roughness in shape (Nicholson et al., 2005). However, Kawata's model requires extremely large contrast in the albedo ($A_V \sim 0.0$–0.4 and 0.9 for large and small particles, respectively, for the B ring) to reproduce the observed tilt effect. This seems improbable because ring particles are likely to have surface frost layers (Froidevaux et al., 1981; Poulet and Cuzzi, 2002; Poulet et al., 2003) and the surface materials are likely to be exchanged between particles by frequent mutual collisions.

In Kawata's model (Kawata and Irvine, 1975; Kawata, 1983), he considers only averaged temperatures for the illuminated and unilluminated hemispheres, and the equator which distinguishes these two hemispheres is assumed to be always parallel to the orbital plane in order to simplify the calculation of the mutual heating flux. The latter would not be a good approximation for slowly rotating particles, since the Sun does not illuminate the Saturn's rings vertically. In addition, the multiple scattering of visible light is ignored in his model.

In the present paper, we will investigate whether our model, which includes three new effects explained above (full radiative transfer calculation of multiple scattering and mutual heating, distribution of spins, and heat transfer via particle motions), can reproduce the observed thermal tilt effect without the vertical heterogeneity of the albedo. In our subsequent paper (Morishima et al., in preparation), we will apply our model to the observations by the Cassini composite infrared spectrometer (CIRS; Flasar et al., 2005; Spilker et al., 2006). In Section 2, we explain our model. The properties of ring temperatures with various parameters are shown in Section 3. In Section 4, we fit our model temperatures to the observed temperatures. Unfortunately, we can not obtain exact values of physical parameters, such as the albedo, fraction of fast rotators, and thermal inertia, due to degeneracy among them. Alternatively, we derive possible combinations of these physical parameters. In Section 5, some additional constraints on the physical parameters from other observations and models are discussed. Our conclusions are given in Section 6.

2. A model

2.1. Assumptions

In our model, we introduce following assumptions:

1. We adopt a multilayer approximation, in which the energy transfer by light is described by the equation of classical radiative transfer (e.g., Chandrasekhar, 1960). This is valid when the distance between particles is much larger than the particles size (See Section 1 for more details).
2. We consider locally uniform rings in the horizontal directions and apply the plane-parallel approximation. The distribution of orbital inclinations of particles in each size is given by the Rayleigh distribution, which corresponds to the Gaussian distribution of the spatial density of ring particles in the vertical direction. These assumptions are valid for optically thin rings (Lissauer and Stewart, 1993; Ohtsuki and Emori, 2000). For optically thick rings, in fact, the distribution deviates from the Rayleigh distribution (Wisdom and Tremaine, 1988; Salo, 1991; Richardson, 1994; Ohtsuki and Emori, 2000) and rings are no longer uniform in the horizontal directions because of self-gravitational wakes or axisymmetric oscillations caused by viscous overstability (Salo, 1992b, 1995; Salo et al., 2001).
3. We consider visible and infrared light integrated over wavelengths in each range when we solve the equation of radiative transfer. Since the emission from the Sun is dominated by visible light, we can treat the Planck function for the Sun's temperature as the intensity of visible light. Similarly, we can treat the Planck function for the temperature of Saturn or ring particles as the intensity of infrared light. We assume the infrared albedo to be zero, so we do not consider the scattered infrared light. The actual value of the infrared albedo is likely to be $\sim$0.1 (Irvine and Pollack, 1968; Kawata and Irvine, 1975; Hudgins et al., 1993; Vokrouhlický et al., 2007).
4. We represent a size distribution of ring particles by a bimodal distribution consisting of fast spinning small particles and non-spinning large particles. We conventionally call them fast and slow rotators, respectively. The scale height of small particles is larger than that of large particles. The thermal structure of a fast spinning particle is assumed to be spherically symmetric.

2.2. Vertical structure of a ring

First we consider the vertical structure of a ring for the case of single-sized particles. The formulation will be easily extended to the case of the bimodal size distribution. The Rayleigh distribution function $f(i)$ of the orbital inclination i is given by

$$f(i) = \frac{2i}{\langle i^2 \rangle} \exp\left(-\frac{i^2}{\langle i^2 \rangle}\right), \tag{1}$$

where $\langle i^2 \rangle$ represents the mean square value of i of particles, and the distribution function is normalized as $\int_0^\infty f(i)\,di = 1$. Assuming $\langle i^2 \rangle^{1/2} \ll 1$, the equations for particle motion in the azimuthal and vertical directions are given by

$$\begin{aligned} \phi_p(t) &= \Omega_K t + \phi_p(t=0), \\ z_p(t) &= \begin{cases} ai\sin(\phi_p(t) - \varpi_p) & \text{(for the A and C rings)}, \\ \pm ai|\sin(\phi_p(t) - \varpi_p)| & \text{(for the B ring)}, \end{cases} \end{aligned} \tag{2}$$

where $\phi_p(t)$ and $z_p(t)$ are the azimuthal and vertical positions of the particle at the time of t (we set $\phi_p = 0$ at the midnight in the Saturn's shadow, and $z_p > 0$ for the side illuminated by the Sun), Ω_K is the orbital frequency of the particle, a is the distance of the particle from the Saturn's center, and ϖ_p is the longitude of ascending node. Ring particles are assumed to distribute randomly with respect to ϖ_p. For the optically thick B ring, the sinusoidal vertical motion is hindered by frequent mutual impacts. To model this effect, we assume that the particles are not able to penetrate through the ring but instead rebound at the midplane. We call this the bouncing model. In practice, we replace each particle with a pair of particles whose inclinations are the same but the sign of vertical coordinates are opposite. We briefly examined vertical motion of ring particles using our N-body code (Morishima and Salo, 2006), and found this kind of behaviors of particles, although the actual motion was more complicated.

The Rayleigh distribution of the orbital inclination corresponds to the Gaussian distribution for the spatial density of particles ρ as a function of the vertical position z:

$$\rho(z) = \frac{\Sigma}{\sqrt{\pi}h} e^{-(z/h)^2}, \tag{3}$$

where $\Sigma = \int_{-\infty}^{\infty} \rho(z)\,dz$ is the surface density of the ring and $h = a\langle i^2\rangle^{1/2}$ is the scale height of the ring. Using the normal optical depth of the ring $\tau = \Sigma\kappa$, where κ is the opacity assumed to be constant, the normal path optical depth to the vertical location z is given by

$$\xi(z) \equiv \kappa \int_z^{\infty} \rho(z)\,dz = \frac{\tau}{2}\,\mathrm{erfc}(z/h), \tag{4}$$

where $\mathrm{erfc}(z/h)$ is the complementary error function. In order to obtain the value of this function, we use the fitting function given in Press et al. (1986; Chap. 6.2).

For the case of the bimodal size distribution, where we assume that the distribution of the orbital inclination in each size is given by the Rayleigh distribution, $\xi(z)$ is given by the summation of the normal path optical depths of fast and slow rotators, $\xi_{\mathrm{fast}}(z)$ and $\xi_{\mathrm{slow}}(z)$:

$$\begin{aligned}\xi(z) &= \xi_{\mathrm{fast}}(z) + \xi_{\mathrm{slow}}(z)\\ &= \frac{\tau_{\mathrm{fast}}}{2}\,\mathrm{erfc}(z/h_{\mathrm{fast}}) + \frac{\tau_{\mathrm{slow}}}{2}\,\mathrm{erfc}(z/h_{\mathrm{slow}}).\end{aligned} \tag{5}$$

Here, τ_{fast} and τ_{slow} represent the total optical depths of fast spinning particles and slowly spinning particles, respectively ($\tau = \tau_{\mathrm{fast}} + \tau_{\mathrm{slow}}$), and h_{fast} and h_{slow} represent the scale heights of these particle groups. The optical depth fraction of small particles $f_{\mathrm{fast}} = \tau_{\mathrm{fast}}/\tau$ and the ratio of the scale height $h_{\mathrm{r}} = h_{\mathrm{fast}}/h_{\mathrm{slow}}$ are treated as parameters.

Dynamical studies suggest that the ratio of the scale height of the smallest particles to that of the largest particles is typically 2–3 regardless of the width of the size distribution (Salo, 1992a; Ohtsuki, 1999; Morishima and Salo, 2006). In most cases, we adopt $h_{\mathrm{r}} = 3$, although we examine the dependence of the ring brightness temperature on h_{r} (Fig. 11). Fig. 1 shows the vertical profile of a ring for the case of $\tau = 1.5$, $f_{\mathrm{fast}} = 0.5$, and $h_{\mathrm{r}} = 3$. In this figure, the optical depths of fast and slow rotators per unit length,

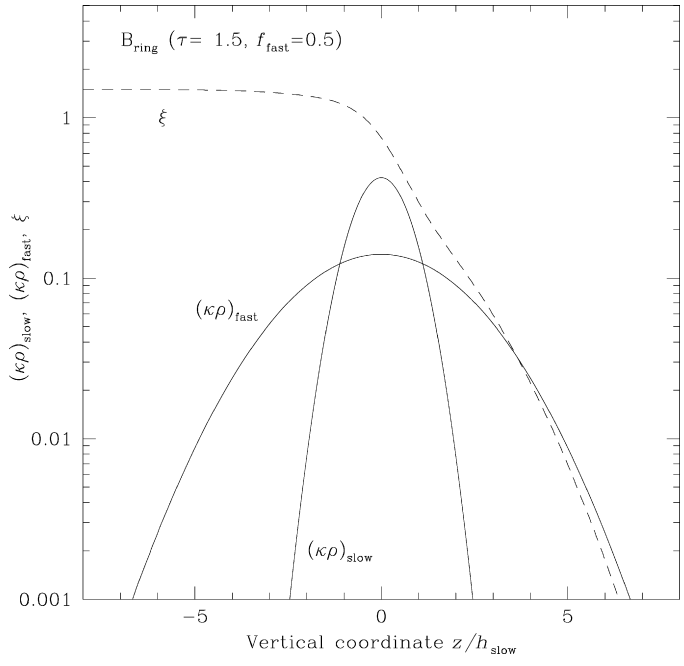

Fig. 1. Vertical profiles of the products of the particle spatial density and opacity for the slow and fast rotators, $(\kappa\rho)_{\mathrm{slow}}$ and $(\kappa\rho)_{\mathrm{fast}}$ in units of h_{slow}^{-1} and the normal pass optical depth ξ to the vertical location z ($d\xi/dz = (\kappa\rho)_{\mathrm{slow}} + (\kappa\rho)_{\mathrm{fast}}$). Here the optical depth τ is 1.5, the fraction of fast rotators f_{fast} is 0.5, and the scale height ratio h_{r} is 3.

$(\kappa\rho)_{\mathrm{fast}}$ and $(\kappa\rho)_{\mathrm{slow}}$, are shown. For the case of fast rotators, we have

$$(\kappa\rho)_{\mathrm{fast}} = d\xi_{\mathrm{fast}}/dz = \tau_{\mathrm{fast}}/\left(\sqrt{\pi}h_{\mathrm{fast}}\right)\exp\left(-(z/h_{\mathrm{fast}})^2\right),$$

and a similar expression is given for slow rotators. Fast rotators are vertically extended so the solar ray is dominantly obscured by fast rotators at $z/h_{\mathrm{slow}} > 1$, in particular, if the solar elevation is low. On the other hand, slow rotators are more concentrated near the midplane. Therefore, an observer mainly sees fast rotators at a small elevation angle, whereas a larger fraction of slow rotators can be seen from an observer at a high elevation angle.

2.3. Radiative transfer

In this section, we derive the intensities due to various heat sources and their solid angles. The intensities and solid angles are used for the calculation of the energy flux to ring particles. The physical temperature of ring particles necessary for the calculation of the intensity due to the mutual heating is obtained by solving the thermal diffusion equation (Section 2.4). The intensities due to the mutual heating and the ring particle temperature are simultaneously solved in iterative procedures (Section 2.5). Using the particle temperatures after convergence, we calculate the observed ring temperatures (Section 2.3.3).

2.3.1. Equation for radiative transfer

The intensity is obtained by solving the equation of radiative transfer (Chandrasekhar, 1960):

$$\mu\frac{dI_k(\xi,\boldsymbol{s},\phi)}{d\xi} = I_k(\xi,\boldsymbol{s},\phi) - S_k(\xi,\boldsymbol{s},\phi), \tag{6}$$

where $\mu = \boldsymbol{s}\cdot\boldsymbol{n}_z$ with the normal direction of the ring plane $\boldsymbol{n}_z$ (note that we defined ξ in Eq. (4) so that it increases with decreasing z), $\boldsymbol{s}$ is the unit vector pointing toward the direction of the ray, ϕ is the azimuthal location in a ring with $\phi = 0$ being the midnight, S is the source function, and the subscript k is V for visible light and IR for infrared light.

The general solution of the equation of radiative transfer is

$$\begin{aligned}I_k^+(\xi,\boldsymbol{s},\phi) &= I_k(\tau,\boldsymbol{s},\phi)e^{-(\tau-\xi)/\mu}\\ &\quad + \int_{\xi}^{\tau} S_k(\xi',\boldsymbol{s},\phi)\exp\left(-\frac{\xi'-\xi}{\mu}\right)\frac{d\xi'}{\mu} \quad (\text{for } 0<\mu<1),\\ I_k^-(\xi,\boldsymbol{s},\phi) &= I_k(0,\boldsymbol{s},\phi)e^{-\xi/|\mu|}\\ &\quad + \int_{0}^{\xi} S_k(\xi',\boldsymbol{s},\phi)\exp\left(-\frac{\xi-\xi'}{|\mu|}\right)\frac{d\xi'}{|\mu|}\\ &\quad (\text{for } -1<\mu<0),\end{aligned} \tag{7}$$

where the first term in the right hand side is the intensity from outside of the ring and the second term is the intensity from surrounding particles. In visible light, the first term corresponds to the direct sunlight $I_{\mathrm{Sun,V}}$ and the sunlight reflected by Saturn $I_{\mathrm{Sat,V}}$ and the second term corresponds to the multiply scattered light $I_{\mathrm{Sca,V}}$. Similarly, in infrared light, the first and second terms correspond to the infrared light from Saturn $I_{\mathrm{Sat,IR}}$ and the mutual heating between ring particles $I_{\mathrm{Mut,IR}}$, respectively.

If a heat source is a black body with a surface temperature T, the intensity emitted from the source, I_0, is given by the product of the emissivity and the Planck function $I_{\mathrm{B}}(T)$, which is integrated over the all wavelengths,

$$I_0 = \epsilon I_{\mathrm{B}}(T) = \epsilon\frac{\sigma_{\mathrm{SB}}T^4}{\pi}, \tag{8}$$

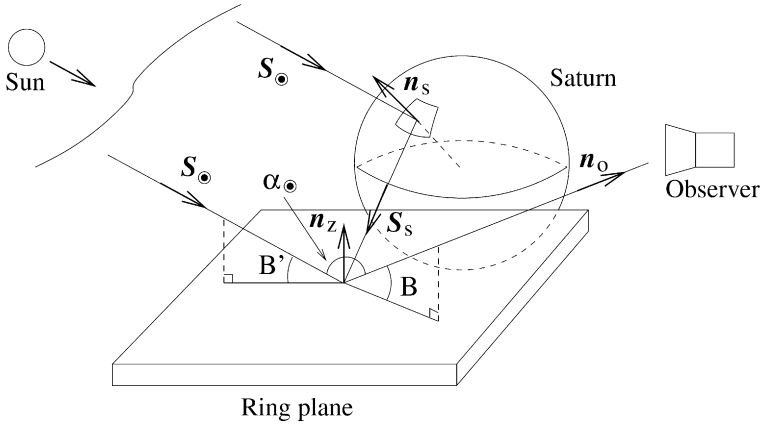

Fig. 2. Geometry of a portion of Saturn's ring and definitions of unit vectors and angles.

where σ_{SB} is the Stefan–Boltzmann constant. We assume that the emissivities of the Sun and Saturn are unity. In most cases in this paper, the emissivity for ring particles is assumed to be unity as well, but we discuss the dependence of ring temperatures on the emissivity in Section 3.4. The values of ϵ for the actual rings are likely to be close to unity (Altobelli et al., 2008).

2.3.2. Heat sources

2.3.2.1. Direct sunlight $I_{Sun,V}$ The direct sunlight and the sunlight reflected by Saturn and other ring particles are eliminated in Saturn's shadow. The azimuth angle at the boundary between the Saturn shadow and illuminated morning side ϕ_b is given by

$$\cos^2\phi_b = \frac{(1-(r_{s,eq}/a)^2)(1-\varepsilon_s\cos^2 B')^2}{(1-\varepsilon_s\cos^2 B')^2-\sin^2 B'}, \tag{9}$$

where $r_{s,eq}$ and ε_s are the equator radius and the oblateness of Saturn assumed to be 60,300 km and 0.1, respectively, and B' is the solar elevation angle. Taking the shadowing of other particles into account, the intensity of the direct sunlight $I_{Sun,V}$ at $\xi(z)$ is given by

$$I_{Sun,V}(\xi,\boldsymbol{s}_\odot,\phi)=\begin{cases} I_B(T_\odot)\exp(-\xi/|\mu_\odot|) & (\text{for } \cos\phi\leqslant\cos\phi_b),\\ 0 & (\text{for } \cos\phi>\cos\phi_b),\end{cases} \tag{10}$$

where $T_\odot$ is the surface temperature of the Sun and $\boldsymbol{s}_\odot$ is the direction of solar ray (see Fig. 2 for definition of vectors) and $\mu_\odot = (-\boldsymbol{s}_\odot)\cdot\boldsymbol{n}_z = \sin B'$.

The solid angle of the Sun $\Omega_\odot$ seen from ring particles at $a_\odot$ from the Sun is given by

$$\int_{\text{Sun}} d\Omega = \Omega_\odot = \frac{\pi r_\odot^2}{a_\odot^2}, \tag{11}$$

where $r_\odot$ is the solar radius. Since the solid angle of the Sun is small enough, the Sun can be treated as a point source. The so-called solar flux is defined as $I_B(T_\odot)\Omega_\odot$, which we use 16.2 W m^{-2} at 9.25 AU after Froidevaux (1981).

2.3.2.2. Thermal and visible radiation from Saturn, $I_{Sat,IR}$ and $I_{Sat,V}$ Since Saturn, unlike the Sun, cannot be treated as a point source, we need to divide the surface of Saturn into facets, and then integrate the intensity over the surface seen from ring particles. The solid angle of a surface facet of Saturn measured from its center is defined to be $d\omega_S$. The solid angle of the facet measured from a ring particle is then given by

$$d\Omega_S(\boldsymbol{s}_S)=\begin{cases} r_S^2|\boldsymbol{n}_S\cdot\boldsymbol{s}_S|\,d\omega_S/d_S^2 & (\text{for } \boldsymbol{n}_S\cdot\boldsymbol{s}_S>0),\\ 0 & (\text{otherwise}),\end{cases} \tag{12}$$

where r_S is the distance between Saturn's center and a facet on the surface (i.e., Saturn's radius), $\boldsymbol{n}_S$ is the unit vector normal to the Saturn's facet, $\boldsymbol{s}_S$ is the unit vector pointing toward the particle from the facet, and d_S is the distance between the particle and the facet (see Fig. 2). The thermal intensity emitted from the surface of Saturn is given by

$$I_{Sat0,IR} = I_B(T_S), \tag{13}$$

where T_S is the surface temperature of Saturn assumed to be 95 K. Assuming a Lambertian surface for Saturn, the intensity of the reflected sunlight is given as

$$I_{Sat0,V}(\boldsymbol{s}_S)=\begin{cases} A_S|\boldsymbol{n}_S\cdot(-\boldsymbol{s}_\odot)|I_b(T_\odot)\Omega_\odot/\pi\\ \quad(\text{for } \boldsymbol{n}_S\cdot(-\boldsymbol{s}_\odot)>0),\\ 0\quad(\text{otherwise}),\end{cases} \tag{14}$$

where A_S is the Bond albedo of Saturn, which is taken as 0.34 (Mullin, 1984). Using Eqs. (13) and (14), the intensities, $I_{Sat,IR}$ and $I_{Sat,V}$, from a facet on Saturn to a particle at ξ are given by

$$I_{Sat,IR}(\xi,\boldsymbol{s}_s,\phi) = I_{Sat0,IR}\exp\left(-\frac{\xi_{ns}}{|\mu_S|}\right), \tag{15}$$

$$I_{Sat,V}(\xi,\boldsymbol{s}_s,\phi) = I_{Sat0,V}\exp\left(-\frac{\xi_{ns}}{|\mu_S|}\right), \tag{16}$$

where $\mu_S = (-\boldsymbol{s}_S)\cdot\boldsymbol{n}_z$, and $\xi_{ns} = \xi$ or $\tau-\xi$ for facets locating on the northern/southern hemisphere of Saturn.

2.3.2.3. Multiple scattering of visible light $I_{Sca,V}$ In Eq. (7), the source function for visible light is given by

$$S_V(\xi',\boldsymbol{s},\phi) = A_V\int_{4\pi} I_V(\xi',\boldsymbol{s}_i,\phi)P_V(\boldsymbol{s},\boldsymbol{s}_i)\frac{d\Omega_i}{4\pi}, \tag{17}$$

where A_V, I_V, P_V are the particle bond albedo, the intensity, and the spherical scattering phase function in visible light, respectively, $\boldsymbol{s}_i$ is the unit vector pointing toward the direction of the incident ray, and $d\Omega_i$ is its solid angle. The bond albedo is defined as

$$A_V = \int_0^\infty A_\lambda I_{B,\lambda}(T_\odot)\,d\lambda \Big/ \int_0^\infty I_{B,\lambda}(T_\odot)\,d\lambda, \tag{18}$$

where A_λ is the particle albedo for a given wavelength λ and $I_{B,\lambda}(T_\odot)$ is the solar intensity per wavelength (i.e., the Planck function at the surface temperature of the Sun, $T_\odot$). Strictly speaking, multi-wavelength calculations are necessary to estimate the intensity of scattered light very accurately, since A_λ strongly depends on λ (e.g., Porco et al., 2005). But that is beyond the scope of the present paper. We assume that P_V is represented by the Lambert sphere phase function (e.g., Salo and Karjalainen, 2003):

$$P_V(\alpha) = \frac{8}{3\pi}\left[\sin\alpha+(\pi-\alpha)\cos\alpha\right], \tag{19}$$

where the phase angle is given as $\alpha = \boldsymbol{s}\cdot(-\boldsymbol{s}_i)$. In fact, the particles in Saturn's rings are likely to be more strongly backward scattering than implied by the Lambert sphere phase function (Dones et al., 1993), so this effect should be investigated in future work.

Substituting Eq. (17) into Eq. (7), and taking the heat sources outside of the ring in visible light into account, we can obtain I_V by an iterative procedure as follows. Replacing I_V and S_V in Eq. (17) by the intensity of nth order scattered light, $I_{V,n}$, and the corresponding source function, $S_{V,n}$, for the next order, respectively, we obtain the relation between $I_{V,n}$ and $I_{V,n+1}$ as

$$I_{V,n+1}(\xi,\boldsymbol{s},\phi) = \begin{cases} \displaystyle\int_{\xi}^{\tau} S_{V,n}(\xi',\boldsymbol{s},\phi)\exp\left(-\frac{\xi'-\xi}{\mu}\right)\frac{d\xi'}{\mu} \\ \quad (\text{for } 0<\mu<1), \\ \displaystyle\int_{0}^{\xi} S_{V,n}(\xi',\boldsymbol{s},\phi)\exp\left(-\frac{\xi-\xi'}{|\mu|}\right)\frac{d\xi'}{|\mu|} \\ \quad (\text{for } -1<\mu<0). \end{cases} \tag{20}$$

The source function in the beginning of iteration, $S_{V,0}$, is obtained by substituting Eqs. (10)–(12), and (16) into Eqs. (17)

$$S_{V,0}(\xi',\boldsymbol{s},\phi) = \frac{A_V}{4\pi}\left(P_V(\boldsymbol{s},\boldsymbol{s}_\odot)I_{\mathrm{Sun},V}\Omega_\odot + \int P_V(\boldsymbol{s},\boldsymbol{s}_S)I_{\mathrm{Sat},V}d\Omega_S\right). \tag{21}$$

It should be noted that substituting Eq. (21) into Eq. (20), the first term in the right hand side is analytically integrable with respect to ξ'. The total intensity of the scattered visible light $I_{\mathrm{Sca},V}$ is given by

$$I_{\mathrm{Sca},V}(\xi,\boldsymbol{s},\phi) = \sum_{n=1} I_{V,n}(\xi,\boldsymbol{s},\phi). \tag{22}$$

The iteration is taken place until $I_{\mathrm{Sca},V}$ sufficiently converges ($I_{V,n}/I_{\mathrm{Sca},V} < 10^{-3}$) for all ξ, $\boldsymbol{s}$, and ϕ. The maximum n necessary for the convergence is ~20 for $\tau = 1.5$ and $A_V = 1$. The maximum n decreases with decreasing τ and A_V.

2.3.2.4. Mutual heating $I_{\mathrm{Mut,IR}}$ As we mentioned in the beginning of Section 2.3, the temperatures of ring particles are obtained by solving the thermal diffusion equation. Details of the calculations are given in Section 2.4. Assuming that the temperatures of ring particles are already given, we here describe the method to obtain the intensity due to the mutual heating.

The intensity emitted from a particle to a certain direction is obtained by integrating the emission over the hemisphere of the particle as

$$S'_{IR}(\xi,\boldsymbol{s},i,\varpi_p,\phi_p) = \frac{1}{\pi}\int_{\text{for }(\boldsymbol{n}_p\cdot\boldsymbol{s})\geqslant 0} \epsilon I_B\big(T_p(\xi,\boldsymbol{n}_p,i,\varpi_p,\phi_p)\big) \times(\boldsymbol{n}_p\cdot\boldsymbol{s})\,d\Omega, \tag{23}$$

where $T_p(\xi(z_p),\boldsymbol{n}_p,i,\varpi_p,\phi_p)$ is the surface temperature of a particle's facet, and $\boldsymbol{n}_p$ is the unit vector normal to the facet. The contribution from a particle to the thermal emission of an ensemble of particles at a certain height, which corresponds to the source function in infrared light in Eq. (7), is proportional to the inverse of the vertical velocity of the particle. With this weight, the source function is then obtained by averaging the temperature over particles with various i's and ϖ_p's at $\phi_p = \phi$

$$S_{IR}(\xi,\boldsymbol{s},\phi) = \frac{\int_0^{2\pi} d\varpi_p/(2\pi)\int_0^\infty di/|\dot{z}_p(\xi,i)|f(i)S'_{IR}(\xi,\boldsymbol{s},i,\varpi_p,\phi_p)\delta(\phi-\phi_p)}{\int_0^{2\pi} d\varpi_p/(2\pi)\int_0^\infty di/|\dot{z}_p(\xi,i)|f(i)\delta(\phi-\phi_p)}, \tag{24}$$

where $f(i)$ is the distribution function of the orbital inclination i (see Eq. (1)), and $\delta(x)$ is unity for $x = 0$ and 0 otherwise. Ideally, we need to use temperatures of particles when they are exactly at $\phi_p = \phi$. In actual simulations with a limited number of particles, however, we use a Gaussian-type function, $\exp[-((\phi-\phi_p)/\Delta\phi)^2]$, instead of $\delta(x)$ for fine sampling with respect to ξ. Unless both ϕ and ϕ_p are either in the shadow of Saturn or in the azimuthal region under the direct solar illumination, the exponential function is set to be zero. We can usually adopt a large value of $\Delta\phi$ (we use $\Delta\phi = 20^\circ$ in the present paper) for observations of the west ansa from the Earth, as the variation of the temperature (or S_{IR}) with respect to ϕ is not large. On the other hand, $\Delta\phi$ needs to be smaller for a good resolution with respect to ϕ, if the temperature variation is large like the case of particles near the shadow boundary. This requires, however, a large number of particles in simulations.

In order to examine the effect of particle's motion, we also consider the static case and the case with vertical motion only at a fixed ϕ. If particles are static ($\dot{z}_p = \dot{\phi}_p = 0$), we can omit the averaging over i and ϖ_p (Eq. (24)) so the source function is obtained by replacing $T_p(\xi(z_p),\boldsymbol{n}_p,i,\varpi_p,\phi_p)$ by $T_p(\xi(z_p),\boldsymbol{n}_p,\phi_p)$ in Eq. (23). In the case of the vertical motion only, we can omit the averaging over ϖ_p in Eq. (24), with $\delta(\phi-\phi_p) = 1$.

For the case of bimodal size distribution, the source function for slow and fast spinning particles, $S_{IR,slow}$ and $S_{IR,fast}$, are individually calculated at a given vertical location using Eqs. (23) and (24). Then, with the weight of the cross section at a given height, $(\kappa\rho)_{slow}(\xi)$ and $(\kappa\rho)_{fast}(\xi)$ (see Fig. 1), the averaged source function is obtained by

$$S_{IR}(\xi,\boldsymbol{s},\phi) = \frac{(\kappa\rho)_{slow}(\xi)S_{IR,slow}(\xi,\boldsymbol{s},\phi)+(\kappa\rho)_{fast}(\xi)S_{IR,fast}(\xi,\boldsymbol{s},\phi)}{(\kappa\rho)_{slow}(\xi)+(\kappa\rho)_{fast}(\xi)}. \tag{25}$$

Finally, the thermal intensity from background particles is obtained from Eq. (25) as

$$I_{\mathrm{Mut,IR}}(\xi,\boldsymbol{s},\phi) = \begin{cases} \displaystyle\int_{\xi}^{\tau} S_{IR}(\xi',\boldsymbol{s},\phi)\exp\left(-\frac{\xi'-\xi}{\mu}\right)\frac{d\xi'}{\mu} \\ \quad (\text{for } 0<\mu<1), \\ \displaystyle\int_{0}^{\xi} S_{IR}(\xi',\boldsymbol{s},\phi)\exp\left(-\frac{\xi-\xi'}{|\mu|}\right)\frac{d\xi'}{|\mu|} \\ \quad (\text{for } -1<\mu<0). \end{cases} \tag{26}$$

For the convenience of later use, we also define the ring physical temperature as

$$T_R(\xi,\boldsymbol{s},\phi) = \left(\frac{\pi S_{IR}(\xi,\boldsymbol{s},\phi)}{\sigma_{SB}\epsilon}\right)^{1/4}. \tag{27}$$

2.3.3. Observed effective and brightness temperatures

There are two types of observed temperatures (Spilker et al., 2005, 2006): the brightness temperature T_b is obtained by directly converting the observed intensity with the Planck function at a certain wavelength, whereas the effective temperature T_{eff} is derived by fitting a ring spectrum to the Planck function in a certain range of wavelength with a scaling factor. The former is usually used for Earth-based observations (Froidevaux, 1981; Kawata, 1983; Lynch et al., 2000; Ferrari et al., 2005), and we also use it in the present paper. On the other hand, the latter is often used for observations by spacecraft (Hanel et al., 1981, 1982; Flasar et al., 2005; Spilker et al., 2005, 2006) and we will use it in our subsequent paper (Morishima et al., in preparation), in which we apply our model to Cassini observations.

We assume that there is no scattering in thermal infrared light and that Saturn is not on the line of sight seen from the observer. The observed intensity is obtained from Eqs. (7) as

$$I^{+}_{\mathrm{IR},\lambda}(\boldsymbol{n}_\mathrm{o},\phi)=\int_0^\tau S_{\mathrm{IR},\lambda}(\xi',\boldsymbol{n}_\mathrm{o},\phi)\exp\left(-\frac{\xi'}{\mu_\mathrm{o}}\right)\frac{d\xi'}{\mu_\mathrm{o}}$$
$$(\text{for } 0<\mu_\mathrm{o}<1),$$
$$I^{-}_{\mathrm{IR},\lambda}(\boldsymbol{n}_\mathrm{o},\phi)=\int_0^\tau S_{\mathrm{IR},\lambda}(\xi',\boldsymbol{n}_\mathrm{o},\phi)\exp\left(-\frac{\tau-\xi'}{|\mu_\mathrm{o}|}\right)\frac{d\xi'}{|\mu_\mathrm{o}|}$$
$$(\text{for } -1<\mu_\mathrm{o}<0), \tag{28}$$

where $\boldsymbol{n}_\mathrm{o}$ is the unit vector pointing toward the observer, $S_{\mathrm{IR},\lambda}$ is the λ-dependent source function in thermal infrared obtained from Eqs. (23) and (24) with replacing ϵ and $I_\mathrm{B}(T)$ by the λ-dependent emissivity and Planck function, ϵ_λ and $I_{\mathrm{B},\lambda}(T)$, respectively, and $\mu_\mathrm{o}=\boldsymbol{n}_\mathrm{o}\cdot\boldsymbol{n}_\mathrm{z}=\sin B$, where B is the elevation angle of the observer. We assume that ϵ_λ is independent of λ.

Using the observed intensity, the brightness temperature T_b is given by

$$I_{\mathrm{IR},\lambda}(\boldsymbol{n}_\mathrm{o},\phi)=I_{\mathrm{B},\lambda}\big(T_\mathrm{b}(\boldsymbol{n}_\mathrm{o},\phi)\big). \tag{29}$$

The dependence of $I_{\mathrm{B},\lambda}(T)$ on T is strong around 20 μm, where most Earth-based observations have been carried out, and with a typical ring temperature, ∼90 K,

$$\frac{d\ln I_{\mathrm{B},\lambda}(T)}{d\ln T}=\gamma\frac{e^\gamma}{e^\gamma-1}\simeq\gamma$$
$$=\frac{h_\mathrm{P}c}{\lambda k_\mathrm{B}T}=8.0\left(\frac{\lambda}{20\ \mu\mathrm{m}}\right)^{-1}\left(\frac{T}{90\ \mathrm{K}}\right)^{-1}, \tag{30}$$

while $d\ln I_\mathrm{B}(T)/d\ln T=4$. In the above, h_P is the Planck constant, c is the speed of light, and k_B is the Boltzmann constant. In the present paper, we will concentrate our attention on 20 μm observations as previous models (Froidevaux, 1981; Kawata, 1983). However, we will discuss the dependence of T_b on λ in Section 3.4.

The effective temperature T_eff is derived from the ring spectrum $I_{\mathrm{IR},\nu}$ (where ν is the wave number) such that

$$I_{\mathrm{IR},\nu}(\boldsymbol{n}_\mathrm{o},\phi)=\beta I_{\mathrm{B},\nu}\big(T_\mathrm{eff}(\boldsymbol{n}_\mathrm{o}),\phi\big), \tag{31}$$

where $I_{\mathrm{B},\nu}$ is the wave-number dependent Planck function ($I_{\mathrm{B},\nu}\,d\nu=-I_{\mathrm{B},\lambda}\,d\lambda$) and β is a scaling factor. For each spectrum, β and T_eff are simultaneously derived as the values minimize the weighted residuals $R(T_\mathrm{eff},\beta)$ between the spectrum and a theoretical spectrum defined by Eq. (31)

$$R(T_\mathrm{eff},\beta)=\sum_\nu\left[\big(I_{\mathrm{IR},\nu}-\beta I_{\mathrm{B},\nu}(T_\mathrm{eff})\big)/\sigma_\nu\right]^2, \tag{32}$$

where σ_ν is the instrument noise equivalent spectral radiance. Three effects are taken into account by the β factor (Altobelli et al., 2007): (1) the geometrical filling factor, which is given by $\beta_f=1-\exp(-\tau/|\mu_\mathrm{o}|)$ in the multilayer approximation, (2) the infrared emissivity ϵ, and (3) the scalar factor β_c that can occur from observing a system comprised of particles at more than one temperature. Then, the β factor is given as

$$\beta=\beta_f\beta_c\epsilon. \tag{33}$$

Since β_f (or the optical depth) and ϵ are given parameters in our numerical simulations, β_c and T_eff are simultaneously derived from Eq. (32), assuming $\sigma_\nu=1$. The spectral region between 100 and 400 cm^{-1} (100–25 μm) is used following the analysis of the CIRS data (Spilker et al., 2006). This range well encompasses the wavelength of the peak intensity.

2.4. Heat balance for a particle

Because of motion of a particle in the vertical and azimuthal directions, the energy flux to the particle changes with time. In order to follow the change of the particle temperature $T_\mathrm{p}(\xi(z_\mathrm{p}),\boldsymbol{n}_\mathrm{p},i,\varpi_\mathrm{p},\phi_\mathrm{p})$ with time, we numerically solve the thermal diffusion equation (Aumann and Kieffer, 1973):

$$\frac{\partial T_\mathrm{p}}{\partial t}=\frac{K}{\rho_\mathrm{p}C}\frac{1}{r^2}\frac{\partial}{\partial r}\left(r^2\frac{\partial T_\mathrm{p}}{\partial r}\right), \tag{34}$$

where K is the thermal conductivity, ρ_p is the internal density, and C is the heat capacity of the particle. We use the Crank–Nicholson method for numerical calculations of the diffusion equation (Press et al., 1986, Chap. 19.2).

The time in the diffusion equation can be normalized by the inverse of the frequency of the illumination change $\omega^{-1}=\Omega_\mathrm{K}^{-1}$. The length can be normalized by the thermally affected skin depth $l_\mathrm{s}(\omega)$ given by

$$l_\mathrm{s}(\omega)=\sqrt{\frac{K}{\rho_\mathrm{p}C\omega}}=\frac{\Gamma}{\rho_\mathrm{p}C\sqrt{\omega}}$$
$$\simeq 1.3\times10^{-3}\left(\frac{\Gamma}{6\ \mathrm{J\,m^{-2}\,K^{-1}\,s^{-1/2}}}\right)\left(\frac{\rho_\mathrm{p}}{450\ \mathrm{kg\,m^{-3}}}\right)^{-1}$$
$$\times\left(\frac{C}{760\ \mathrm{J\,kg^{-1}\,K^{-1}}}\right)^{-1}\left(\frac{2\pi/\omega}{10\ \mathrm{h}}\right)^{1/2}\ \mathrm{m}, \tag{35}$$

where $\Gamma=\sqrt{\rho_\mathrm{p}CK}$ is the thermal inertia. In the above, we used plausible values for physical parameters, although they still have some uncertainties. Because of voids, ρ_p is likely to be smaller than that for the density of solid ice (900 $\mathrm{kg\,m^{-3}}$), but N-body simulations using too small ρ_p (say, <300 $\mathrm{kg\,m^{-3}}$) cannot reproduce wake structures seen in the A and B rings (Salo, 1995, Salo et al., 2001). The substituted value of C (= 760 $\mathrm{J\,kg^{-1}\,K^{-1}}$) is a typical value for water ice around 100 K (Schulman, 2004). The thermal inertia of particles in Saturn's rings estimated from the rate of temperature increase in the post-eclipse heating is 2–30 $\mathrm{J\,m^{-2}\,K^{-1}\,s^{-1/2}}$ (Froidevaux et al., 1981; Ferrari et al., 2005; Leyrat et al., 2008). The thermal conductivity K estimated from the above ρ_p, C, and Γ is 10^{-5}–10^{-3} $\mathrm{W\,m^{-1}\,K^{-1}}$, which is consistent with the value for the ice frost (Kouchi et al., 1992). The orbital period is about 10 h at the location of the B ring. Taking these expected values into account, $l_\mathrm{s}(\Omega_\mathrm{K})$ is likely to be even smaller than the size of the smallest ring particles (∼ cm; French and Nicholson, 2000). Therefore, we only calculate the thermal evolution of the surface layer of a particle with a sufficiently large thickness $7l_\mathrm{s}(\Omega_\mathrm{K})$, assuming $R\gg l_\mathrm{s}$, where R is the particle radius (strictly speaking, this assumption would not be appropriate for the smallest particles).

Then, we give the inner boundary condition for Eq. (34) as

$$\left.\frac{\partial T_\mathrm{p}}{\partial r}\right|_{r=R-7l_\mathrm{s}}=0. \tag{36}$$

The boundary condition at the surface of the particle is given as

$$K\left.\frac{\partial T_\mathrm{p}}{\partial r}\right|_{r=R}=F_\mathrm{total}-\epsilon\sigma_\mathrm{SB}T_\mathrm{p}^4, \tag{37}$$

where F_total is the total radiation flux received at the surface of the particle.

The total radiation flux F_total in Eq. (37) consists of the direct solar radiation $F_{\mathrm{Sun,V}}$, the thermal radiation from Saturn $F_{\mathrm{Sat,IR}}$, the reflected sunlight by Saturn $F_{\mathrm{Sat,V}}$, the heating by nearby particles $F_{\mathrm{Mut,IR}}$, and the multiple scattering of visible light by neighboring particles $F_{\mathrm{Sca,V}}$:

$$F_\mathrm{total}=F_{\mathrm{Sun,V}}+F_{\mathrm{Sat,V}}+F_{\mathrm{Sca,V}}+F_{\mathrm{Sat,IR}}+F_{\mathrm{Mut,IR}}. \tag{38}$$

Any flux in the right-hand side of Eq. (38) received by a certain facet of the particle at the vertical location z_p, where the path optical depth is $\xi(z_p(t))$, and the azimuthal location $\phi_p(t)=\phi$ is obtained by integrating the intensity of a heat source I_k over its solid angle as

$$F_k(\xi,\boldsymbol{n}_p,\phi)=\frac{1}{4}(1-A_k)\int_{\text{heat source}}\Phi(\boldsymbol{n}_p,\boldsymbol{s})I_k(\xi,\boldsymbol{s},\phi)\,d\Omega, \tag{39}$$

where A_k is the particle Bond albedo (A_V is from Eq. (18) and $A_{IR}=0$), the subscript k is V for visible light or IR for infrared light, $\Phi(\boldsymbol{n}_p,\boldsymbol{s})$ is the spin function defined below, and $d\Omega$ is the solid angle of the heat source seen from the particle. The spin function is given as

$$\Phi(\boldsymbol{n}_p,\boldsymbol{s})=\begin{cases}\text{Max}(-4\cos(\boldsymbol{n}_p\cdot\boldsymbol{s}),0)\\ \quad\text{(for non-spinning particles)},\\ 1\quad\text{(for fast spinning particles)}.\end{cases} \tag{40}$$

The spin function is normalized as $\int\Phi\,d\Omega=4\pi$ and the factor $1/4$ in Eq. (39) comes from the normalization.

For the case of the direct sunlight, since the solid angle of the Sun is small enough, we can put Φ and $I_{\text{Sun,V}}$ outside of the integrand in Eq. (39). Then, $F_{\text{Sun,V}}$ is obtained from Eqs. (10) and (11) as

$$F_{\text{Sun,V}}(\xi,\boldsymbol{n}_p,\phi)=\frac{1}{4}(1-A_V)\Phi(\boldsymbol{n}_p,\boldsymbol{s}_\odot)I_{\text{sun,v}}(\xi,\boldsymbol{s}_\odot,\phi)\Omega_\odot. \tag{41}$$

The fluxes from Saturn are obtained by integrating the intensity over the solid angle of Saturn using Eqs. (12), (15), and (16):

$$F_{\text{Sat,IR}}(\xi,\boldsymbol{n}_p,\phi)=\frac{1}{4}\int\Phi(\boldsymbol{n}_p,\boldsymbol{s}_S)I_{\text{Sat,IR}}(\xi,\boldsymbol{s}_s,\phi)\,d\Omega_S, \tag{42}$$

$$F_{\text{Sat,V}}(\xi,\boldsymbol{n}_p,\phi)=\frac{1}{4}(1-A_V)\int\Phi(\boldsymbol{n}_p,\boldsymbol{s}_S)I_{\text{Sat,V}}(\xi,\boldsymbol{s}_s,\phi)\,d\Omega_S. \tag{43}$$

Similarly, the flux due to multiple scattering of visible light $F_{\text{Sca,V}}$ and the mutual heating flux $F_{\text{Mut,IR}}$ can be obtained by substituting Eqs. (22) and (26) into Eq. (39), respectively.

When we solve the thermal diffusion equation, the total flux F_{Total} is interpolated between mesh points with respect to z and ϕ. At the mesh points of the shadow boundaries ($\phi=\phi_b$ and $2\pi-\phi_b$), we calculate F_{Total} for both the cases with and without the fluxes in visible light. Then, the interpolation is independently done in the shadow of Saturn and the azimuthal region directly illuminated by the Sun.

If the energy flux to a particle is periodic as in the present case, the temperature of the particle will be periodic as well after it reaches to its thermal equilibrium state. In the thermal equilibrium state, the energy flux to the particle balances with the thermal flux emitted by the particle when averaged over the orbital period. It should be noted that the surface temperature variation with time only depends on the thermal inertia Γ in such a case, as long as $R\gg l_s$. The time necessary to reach to the thermal equilibrium state is characterized by the thermal relaxation time τ_{rel} given by (Farinella et al., 1998)

$$\begin{aligned}\tau_{\text{rel}}&=\frac{\Gamma}{\epsilon\sigma_{SB}T_p^3\sqrt{\omega}},\\ &=1.1\times10^4\epsilon^{-1}\left(\frac{\Gamma}{6\ \text{J m}^{-2}\,\text{K}^{-1}\text{s}^{-1/2}}\right)\\ &\quad\times\left(\frac{T_p}{90\ \text{K}}\right)^{-3}\left(\frac{2\pi/\omega}{10\ \text{h}}\right)^{1/2}\text{s}.\end{aligned} \tag{44}$$

The possible range of T_p for Saturn's rings is 40–130 K: the minimum value is the case with the thermal emission from Saturn only at the location of the A ring while the maximum value is the case of the subsolar point of a non-spinning particle with $A_V=0$ and without any shadows. Therefore, τ_{rel} can be shorter or longer than the orbital period ($\tau_{\text{orb}}=2\pi/\Omega_K$) for high and low T_p, respectively. Besides the condition from τ_{rel}, at least a few orbital periods are necessary for the thermal equilibrium over an orbital period. After some numerical experiments, we found that the following integration time T_{int} is necessary for the thermal equilibrium:

$$T_{\text{int}}=\text{Max}\big(5\tau_{\text{orb}},2\tau_{\text{rel}}(T_{\text{p,mean}})\big), \tag{45}$$

where $T_{\text{p,mean}}$ is the temperature averaged over ξ and $\boldsymbol{s}_s$ at the west ansa ($\phi=270°$). Ideally, the temperature used for the estimation of τ_{rel} should be the minimum temperature with respect to ξ, $\boldsymbol{s}_s$, and ϕ, but such a severe condition is usually unnecessary.

We found that the time step size should be smaller than at least $\sim0.03\tau_{\text{rel}}(T_{\text{p,max}})$ for the stability of the Crank–Nicholson method, where $T_{\text{p,max}}$ is the maximum temperature with respect to ξ, $\boldsymbol{s}_s$, and ϕ. In addition, for a good accuracy, the time step size should be preferably smaller than the thermal diffusion time

$$\tau_{\text{diff}}=(\Delta r)^2/\big[K/(\rho_pC)\big]=\tau_{\text{orb}}\big[\Delta r/\ell_s(\Omega_K)\big]^2/(2\pi)$$

for one mesh size Δr (we adopt $\ell_s/\Delta r=10$). In practice, we adopt the following time step size Δt in our simulations

$$\Delta t=\text{Min}\big(0.001\tau_{\text{orb}},0.02\tau_{\text{rel}}(T_{\text{p,max}})\big). \tag{46}$$

2.5. Numerical procedure

The numerical procedure to obtain the intensities of rings and the physical temperatures of particles is schematically summarized in Fig. 3. The physical parameters which control the thermal field of the ring ($S_{IR}(\xi',\boldsymbol{n}_o,\phi)$) are as follows: the distance from the Saturn center a, the optical depth τ, the fraction of fast spinning particles in the optical depth $f_{\text{fast}}(=\tau_{\text{fast}}/\tau)$, the ratio of the scale height between fast and slow spinning particles h_r, the albedo in visible light A_V, the thermal inertia Γ, the emissivity ϵ, and the solar elevation angle B'.

With these input parameters, we first calculate the direct solar illumination $I_{\text{Sun,V}}$, and the fluxes from Saturn, $I_{\text{Sat,V}}$ and $I_{\text{Sat,IR}}$ (Sections 2.3.2.1 and 2.3.2.2). Using $I_{\text{Sun,V}}$ and $I_{\text{Sat,V}}$ for the initial source function in visible light, the iteration procedure in each azimuthal location gives the intensity due to the multiple scattering light $I_{\text{Sca,V}}$ (Section 2.3.2.3). Note that the above four intensities (intensities except $I_{\text{Mut,IR}}$) are given as a function of the vertical and azimuthal positions and the normal direction of a facet on a ring particle, and do not change regardless of whether particles move or not. Using these four intensities, the temporary energy flux to ring particles F_{total} is calculated from Eq. (39).

Next we calculate the intensity due to mutual heating $I_{\text{Mut,IR}}$ for the case of static particles ($\dot z_p=\dot\phi_p=0$ or $K=0$). In the case of $K=0$, the temperature is simply obtained by

$$T_p(\xi',\boldsymbol{n}_o,\phi)=\big[F_{\text{total}}(\xi',\boldsymbol{n}_o,\phi)/(\epsilon\sigma_{SB})\big]^{1/4}$$

(see Eq. (37)). The temporary intensity $I_{\text{Mut,IR}}$ and flux $F_{\text{Mut,IR}}$ are then calculated from T_p in the procedure described in Section 2.3.2.4 and Eq. (39). Adding the temporary $F_{\text{Mut,IR}}$ to other four fluxes, we obtain the updated F_{total} and T_p. This procedure is repeated until $F_{\text{Mut,IR}}$ and T_p converge. The converged $F_{\text{Mut,IR}}$ and T_p are used as initial guesses in the iteration procedure for moving particles.

Using these initial guesses, we solve the thermal diffusion equation for a moving particle with given i and ϖ_p (Section 2.4). Once the particle reaches to its thermal equilibrium state, in which the illumination flux balances with the radiating flux when averaged over the orbital period, T_p becomes completely periodic with the orbital period. Using T_p's of particles with various i's and ϖ_p's after they reach to the thermal equilibrium state, we

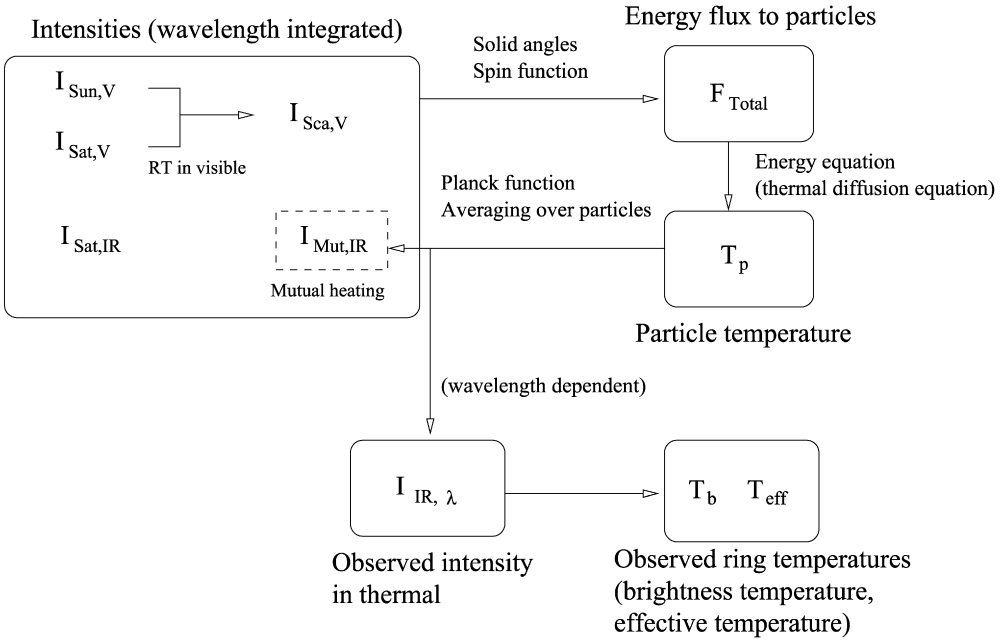

Fig. 3. Flow chart for the numerical procedure to obtain observed ring temperatures. We assume that the albedo in thermal light is zero so the scattered thermal light is ignored.

calculate a new source function in infrared light $S_{IR}(\xi', \boldsymbol{n}_o, \phi)$ and new $F_{Mut,IR}(\xi', \boldsymbol{n}_o, \phi)$, following the procedure described in Section 2.3.2.4. Using the updated flux, we solve the temperature evolution of particles again. This procedure is repeated until $F_{Mut,IR}(\xi', \boldsymbol{n}_o, \phi)$ converges.

We adopt the condition of the convergence in both cases of moving and static particles as $|\Delta F_{Mut,IR}|/F_{Mut,IR} < 5 \times 10^{-3}$ for all $\xi, \boldsymbol{n}_p$, and ϕ, where $\Delta F_{Mut,IR}$ is the deviation of $F_{Mut,IR}$ from the last iteration. This guarantees an error due to iteration to be less than ~0.2 K. For static particles, we usually need a much larger number of iterations than that in the case of moving particles (typically ~50 and 5 for the former and latter cases, respectively, for $\tau = 1.5$). This follows from the inefficient heat transport due to the thermal radiation only. Note that, however, the computational time required in numerical calculations for static particles is much shorter than for moving particles, because most of the time is consumed in solving the thermal diffusion equation for the latter case.

Once the thermal field (S_{IR}) converges, we can obtain the observed brightness and effective temperatures with a given solar phase angle $\alpha_\odot$ (or a saturnocentric longitude of the observer) and observer elevation angle B (Eqs. (29) and (32) in Section 2.3.3). Note that we consider only the case with $\alpha_\odot = 0$ (thus $B = B'$) in the present paper except when obtaining unlit side temperatures.

Besides physical parameters listed in the beginning of Section 2.5, there are some other numerical parameters in our simulations. In a standard case, we used following parameters: the grid number for z ($-9 \leqslant z/h_{slow} \leqslant 9$) is 600, the grid number for ϕ is 10, the number of rays for radiative transfer (thus number of particle facets) is 60, the grid number for i ($0 < ai/h \leqslant 3$) is 20 for each of slow and fast rotators, the grid number for ϖ_p ($0 \leqslant \varpi_p < 2\pi$) is 20, and the mesh number for the surface layers of each particle is 70. The facets of a pentakis dodecahedron (with 60 faces) is used so that solid angles of all facets are equal. For the case of the bouncing model, we double the number of particles. From the calculations with different numbers of grids or particles, the numerical error in the brightness temperature is estimated to be less than 1 K in most cases. Note that finer grids in the z direction are required in the case of smaller B' as we need to accurately solve the thermal structure of thin and warm upper layers of the ring.

3. Dependence of ring temperatures on various physical parameters

In this section, we show some basic properties of ring temperatures in cases with various physical parameters. The precise data fit to the observed temperatures will be done in Section 4.

3.1. Effect of particle motion

Fig. 4 shows an example of trajectories of particles on the T_p vs. z/h_{fast} plane for the case of the B ring-like parameters: $\tau = 1.5$, $f_{fast} = 1.0$, $A_V = 0.7$, $a = 100{,}000$ km, with $B' = 2°$. Only particles' vertical motion is taken into account at the west ansa, and their azimuthal motion is not included (see Section 2.3.2.4). Note that here all particles are assumed to be fast rotators for simplification so there is no dependence of T_p on the normal direction of the facet. As shown in the figure, trajectories are closed after particles reach to its thermal equilibrium state, in which the illumination flux balances with the radiation flux when averaged over the orbital period. In Fig. 4, we also plot the vertical profile of the ring physical temperature, $T_R(z)$ (Eq. (27)), in the first iteration and that after convergence. One can see the heat transport from warmer parts to colder parts and that the heat transport is less efficient for the bouncing model than the standard model with the sinusoidal vertical motion. The temperature is coldest around the midplane, since particles with small i's are concentrated near the midplane and the direct solar illumination can hardly reach to them.

The dependence of the observed brightness temperature $T_{b,v}$ on thermal inertia Γ is shown in Fig. 5 (the subscript v denotes the case with vertical motion only). Since the Sun's illumination mostly attenuates around the vertical location where $\xi(z)/\sin|B'| \sim 1$ for the optically thick rings, only upper layers with large z/h_{fast} are directly heated by the Sun (see Fig. 4). From the Earth, we mainly observe these heated layers. Since ring particles transfer thermal energy from the illuminated side to the unilluminated side, the temperature observed from the Earth decreases with increasing efficiency of the heat transport (i.e. larger Γ). The cooling of the upper layers is more enhanced for smaller $|B'|$ owing to the increase of the shadowed layers, where the Sun's illumination cannot directly reach.

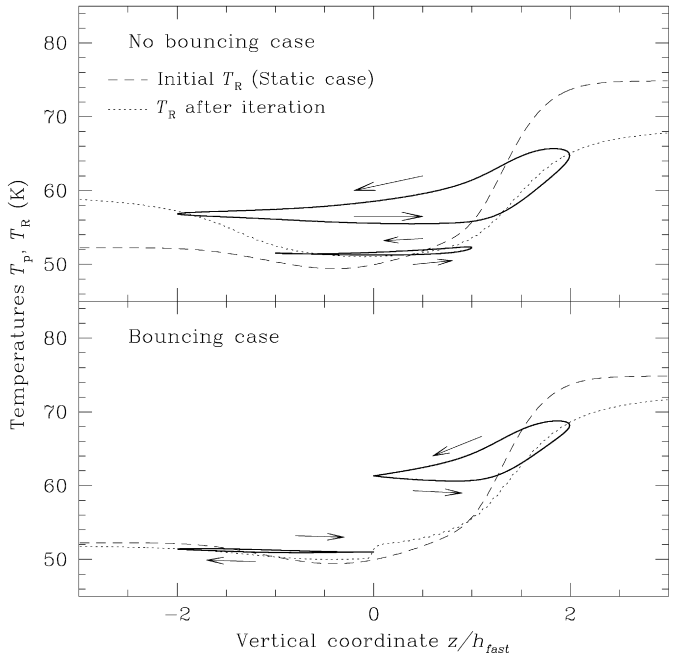

Fig. 4. Particle trajectories on the T_p vs. z/h_{fast} plane for $\tau = 1.5$, $A_V = 0.7$, $f_{fast} = 1.0$, $a = 100{,}000$ km, $\Gamma = 6\ J m^{-2} K^{-1} s^{-1/2}$, and $B' = 2°$. Upper panel: Particle vertical motion is standard sinusoidal (see Eq. (2)), and the cases for $ai/h_{fast} = 1.0$ and 2.0 are shown. Lower panel: Particles are assumed to bounce at the midplane of the ring, and two trajectories with the same ai/h_{fast} (= 1.0) but different signs of z are shown. The long-dashed line in each panel is the temperature profile of the ring with static particles used as an initial guess for the iteration for moving particles and the short-dashed line is the temperature profile with the vertical motion of particles converged after the iteration. Trajectories shown here are obtained with using the thermal flux from static particles (or in the first iteration).

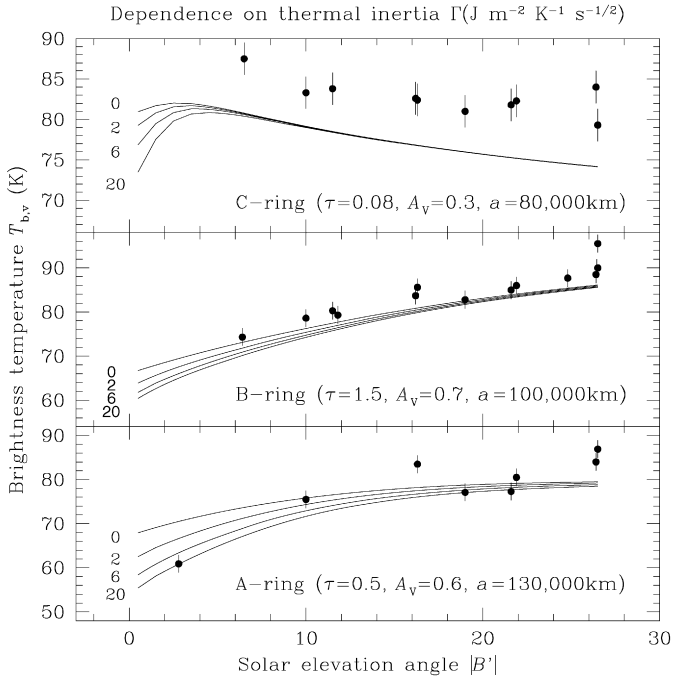

Fig. 5. Brightness temperature as a function of the solar elevation angle for different values of the thermal inertia, Γ. The numbers indicate values of the thermal inertia in units of $J m^{-2} K^{-1} s^{-1/2}$. Here all particles are assumed to be fast rotators ($f_{fast} = 1.0$). The particle motion only in the vertical direction is taken into account at $\phi = 270°$. For the B ring, the vertical motion is given by the bouncing model, whereas the standard sinusoidal motion is assumed for the C and A rings (see Eq. (2)). The filled dots are observed temperatures from Table 1 (see Section 4.1).

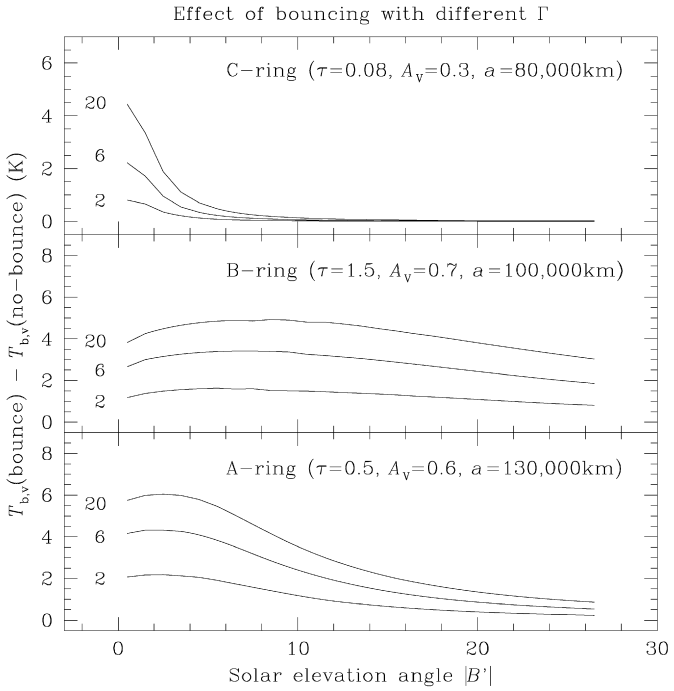

Fig. 6. Effect of the bouncing motion. The deviation of the brightness temperature for the case of the bouncing model from that for the case with the standard sinusoidal motion is shown. The numbers indicate values of the thermal inertia in units of $J m^{-2} K^{-1} s^{-1/2}$. Only the vertical motion is taken into account at $\phi = 270°$ (the west ansa) with $f_{fast} = 1.0$.

The temperature drop due to the vertical heat transport depends on τ. For the C ring, the vertical heat transport is insignificant, since the sunlight reaches to any vertical location and the temperature variation in the vertical direction is small, except at very small $|B'|$. With increasing optical depth, the temperature drop due to the vertical motion increases even for larger $|B'|$, as long as particles follow the sinusoidal motion. However, the prevention of the sinusoidal motion due to mutual collisions also increases with optical depth. Note that we adopt the bouncing model for the B ring but not for the A ring. As a result, the temperature drop due to the vertical motion is larger in the A ring than the optically thicker B ring.

The effect of the bouncing at the midplane is more clearly shown in Fig. 6. The figure shows the difference in the brightness temperatures between the bouncing model and the standard model with the sinusoidal motion. As can be seen, the deviation increases with increasing $\tau/\sin|B'|$, except for very large $\tau/\sin|B'|$, since the effect of the vertical heat transport is more enhanced with increasing attenuation of the direct illumination except upper layers. When $\tau/\sin|B'|$ is very large (>10), the ring physical temperature around the midplane is so low that the directly illuminated upper layers can cool significantly even when the vertical motion of particles is restricted to $z > 0$. Therefore, the deviation in Fig. 6 does not increase any more at very large $\tau/\sin|B'|$.

The effect of the azimuthal motion of particles is insignificant as compared with that of the vertical motion, at least, for the ring temperature at the west ansa seen form the Earth. Fig. 7 shows the difference in the brightness temperatures between the case including the azimuthal motion T_b and the case with vertical motion only $T_{b,v}$. There are two factors causing the difference. The first one is the eclipse cooling, which decreases the ring temperature. This effect is small at the west ansa because of the subsequent heating of particles emerging from the Saturn's shadow. However, if the thermal relaxation

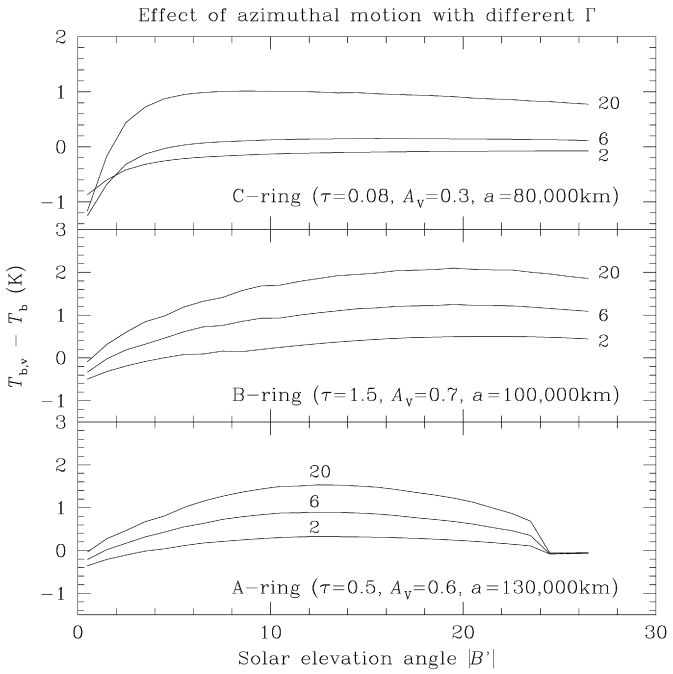

Fig. 7. Effect of azimuthal motion. Difference in brightness temperature between the case with the vertical motion only and from the case including the azimuthal motion is shown. The numbers indicate values of the thermal inertia in units of $\mathrm{J\,m^{-2}\,K^{-1}\,s^{-1/2}}$. All particles are assumed to be fast rotators.

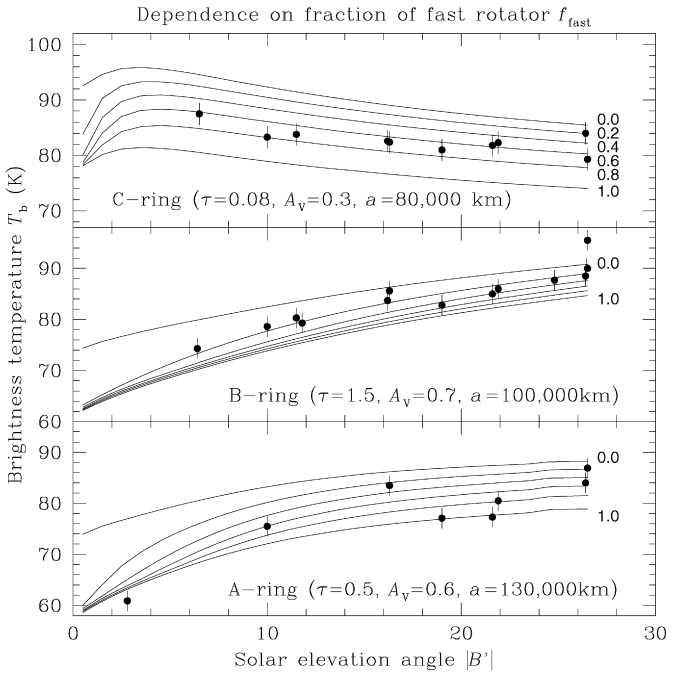

Fig. 8. Brightness temperature as a function of solar elevation angle for different values of the fraction of fast rotators, f_{fast}, between 0.0 to 1.0 with the interval of 0.2. The numbers indicate values of f_{fast}. The thermal inertia is $6\ \mathrm{J\,m^{-2}\,K^{-1}\,s^{-1/2}}$.

time is not short enough in case with a large Γ, as compared with the duration of the heating, the temperature drop due to the eclipse cooling cannot be ignored even at the west ansa.

The second factor is the asymmetry of the fluxes from Saturn. For the case of Fig. 7, in which we assume all particles to be fast rotators, the asymmetry of the Saturn's flux is caused by the reflected sunlight, which is largest at the noon ($\phi = 180°$). This effect slightly increases T_{b} at the west ansa, and the contribution from the flux from Saturn is more important at smaller $|B'|$. As can be seen in Fig. 7, the first factor is more important (positive values of $T_{\mathrm{b,v}} - T_{\mathrm{b}}$) at large $|B'|$ while the second factor is relatively more important at smaller $|B'|$. When the solar elevation is close to its maximum, $|B'| \sim 26°$, the A ring is outside of Saturn's shadow at any azimuthal position and the contribution from Saturn's flux is negligible relative to the direct solar flux. As a result, the difference $T_{\mathrm{b,v}} - T_{\mathrm{b}}$ becomes nearly zero. This result also proves the accuracy of our numerical simulations, as $T_{\mathrm{b,v}}$ and T_{b} are obtained by different procedures.

3.2. Effect of vertical heterogeneity of spins of ring particles

Fig. 8 shows the brightness temperature, T_{b}, with various values of the fraction of fast rotators, f_{fast}. In principle, T_{b} decreases with increasing f_{fast} for all the rings, as we anticipated. Another important fact is that T_{b} tends to converge to the case of $f_{\mathrm{fast}} = 1.0$ at small $|B'|$, unless $f_{\mathrm{fast}} = 0.0$.

In order to understand the behavior of T_{b} shown in Fig. 8, we made two supplementary figures, Figs. 9 and 10. Fig. 9 shows the vertical profile of the ring physical temperature, T_{R} (Eq. (27)), with various values of $|B'|$ for the case of $f_{\mathrm{fast}} = 0.2$ and $\boldsymbol{s} = -\boldsymbol{s}_{\odot}$: the ring temperature here is obtained from the averaged emission of ring particles towards the direction of the Sun. At very small $|B'|$, only the upper most layers are directly heated by the Sun and the ring temperature is coldest around the midplane, similarly to the case shown in Fig. 4. With increasing $|B'|$, the direct sunlight starts to reach to the midplane where slow rotators concentrate. This

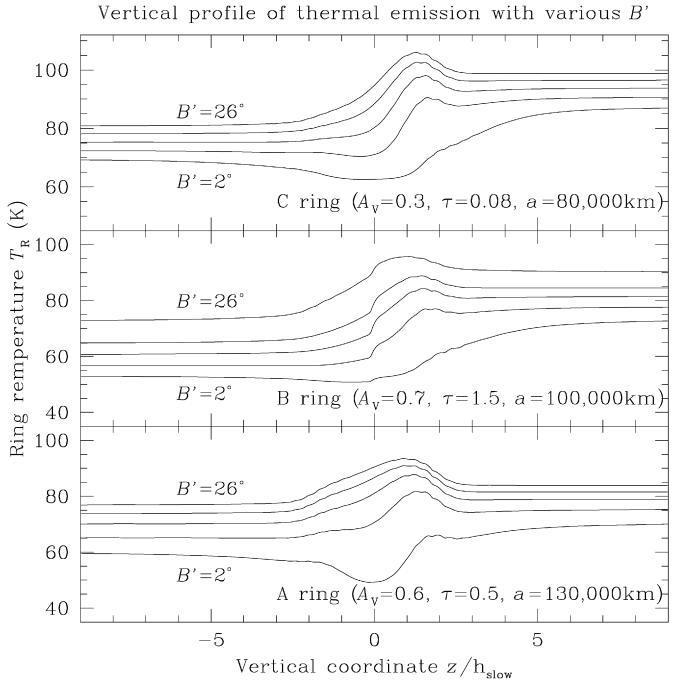

Fig. 9. Vertical profile of the ring temperature, T_{R}, at the subsolar point. The solar elevation angle B' is from 2 to 26° for the bottom to top lines with the interval of four degrees. Here $\Gamma = 6\ \mathrm{J\,m^{-2}\,K^{-1}\,s^{-1/2}}$ and $f_{\mathrm{fast}} = 0.2$.

makes T_{R} near the midplane highest, and the observed brightness temperature significantly increases.

Therefore, the degree of temperate increase with increasing $|B'|$ depends on how large a fraction of slow rotators can be illuminated by the Sun and seen from the observer. We define the effective fraction of fast rotators, $f_{\mathrm{fast,eff}}$, to be the fraction of fast rotators to the normal path optical depth $\xi(z)$ at z where

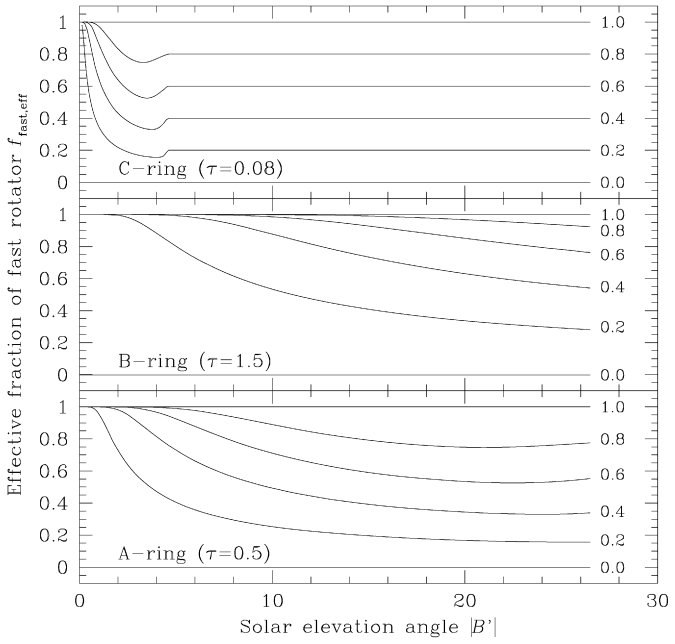

Fig. 10. Effective fraction of fast rotators (Eq. (47)) seen from the Earth for different values of f_{fast} (the number next to each line) between 0.0 to 1.0 with the interval of 0.2.

$\xi(z)/\sin|B'| = 1$ (see Eqs. (4) and (5) for the definition of $\xi(z)$):

$$f_{fast,eff}(\tau, B') = \begin{cases} \dfrac{\xi_{fast}(z)}{\xi(z)} & \left(\text{with } \dfrac{\xi(z)}{\sin|B'|} = 1\right), \\ f_{fast} & \left(\text{for } \dfrac{\tau}{\sin|B'|} < 1\right). \end{cases} \quad (47)$$

This quantity roughly represents the fraction of fast rotators seen from the observer, and the fraction illuminated by the Sun can be obtained by replacing B' by B. Fig. 10 shows $f_{fast,eff}$ as a function of B'. If $\tau/\sin|B'| < 1$ due to small τ and/or large B', the observer can see all particles ($f_{fast,eff} = f_{fast}$). On the other hand, when $\tau/\sin|B'| > 1$, $f_{fast,eff}$ increases to unity with decreasing $\sin|B'|$, unless $f_{fast} = 0$. When $\tau/\sin|B'|$ is only slightly larger than unity, $f_{fast,eff}$ becomes smaller than f_{fast}, since the observer can see most of slow rotators but not fast rotators in the unilluminated side. This explains the dip at $|B'| \sim 4°$ for the C ring.

The value of B' at which $T_b(f_{fast} < 1)$ converges to $T_b(f_{fast} = 1)$ in Fig. 8 is almost the same as the B' value at which $f_{fast,eff}$ converges to unity in Fig. 10. Therefore, the behavior of T_b seen in Fig. 8 can be explained by the effective fraction of fast rotators, $f_{fast,eff}$, seen from the observer. For the A and B rings, the temperature increase with increasing B' is most strongly enhanced for small $f_{fast}(> 0)$. For the optically thin C ring, both fast and slow rotators can be seen regardless of $|B'|$, except for very small $|B'|$. Therefore, the temperature curve of the C ring in Fig. 8 shifts by a nearly constant amount with changing f_{fast} for all $|B'|$'s.

The effect of vertical heterogeneity of particle spins depends on the scale height ratio, $h_r = h_{fast}/h_{slow}$. Fig. 11 shows the deviation of $T_b(h_r)$ from $T_b(h_r = 3)$. If the observer can see all particles ($\tau/\sin|B'| < 1$ or $f_{fast,eff} = f_{fast}$), $T_b(h_r)$ does not depends on h_r. If $\tau/\sin|B'| > 1$, $T_b(h_r)$ increases with decreasing h_r, as the observer can see larger fraction of slow rotators at a certain $\sin|B'|$. When $\tau/\sin|B'|$ is very large, the dependence of $T_b(h_r)$ on h_r becomes weak, since the observer can see only fast rotators in the upper layers. Overall, the dependence of T_b on h_r is not large, as long as $h_r > 2$, which is suggested from dynamical simulations (e.g. Morishima and Salo, 2006).

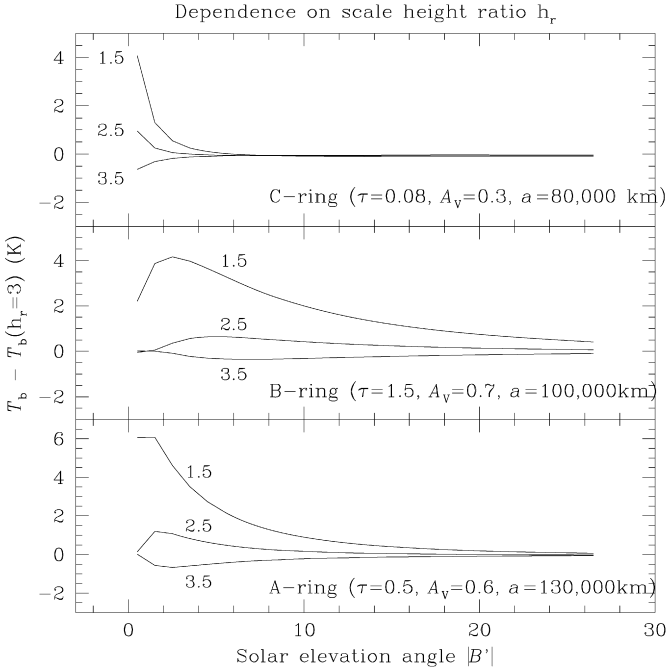

Fig. 11. Dependence of brightness temperature on scale height ratio $h_r = h_{fast}/h_{slow}$. The deviation of T_b from the case of $h_r = 3$ is shown. The numbers indicate values of h_r. Here $\Gamma = 6\,\mathrm{J\,m^{-2}\,K^{-1}\,s^{-1/2}}$ and $f_{fast} = 0.2$.

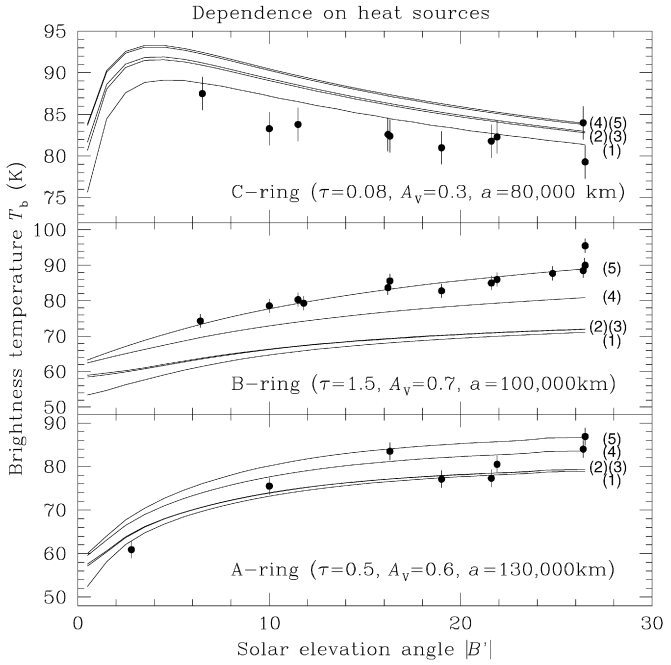

Fig. 12. Effect of different heat sources. The number next to each line indicates contributions from different heat sources: (1) $F_{Sun,V}$, (2) $F_{Sun,V} + F_{Sat,IR}$, (3) $F_{Sun} + F_{Sat,IR} + F_{Sat,V}$, (4) $F_{Sun} + F_{Sat,IR} + F_{Sat,V} + F_{Mut,IR}$, and (5) $F_{Sun} + F_{Sat,IR} + F_{Sat,V} + F_{Mut,IR} + F_{Sca,V}$. Here $F_{Sun,V}$ is the direct illumination flux from the Sun, $F_{Sat,IR}$ and $F_{Sat,V}$ are the fluxes from Saturn in infrared and visible light, and $F_{Mut,IR}$ and $F_{Sca,V}$ are the fluxes from surrounding particles in infrared and visible light. Curves marked with (2) and (3) are top of each other as $F_{Sat,V}$ is very small. We adopt $\Gamma = 6\,\mathrm{J\,m^{-2}\,K^{-1}\,s^{-1/2}}$ and $f_{fast} = 0.2$.

3.3. Contributions from different heat sources

The contributions to the brightness temperature from different heat sources are shown in Fig. 12. The curve marked with (1) corresponds to the case with the direct solar illumination ($F_{Sun,V}$)

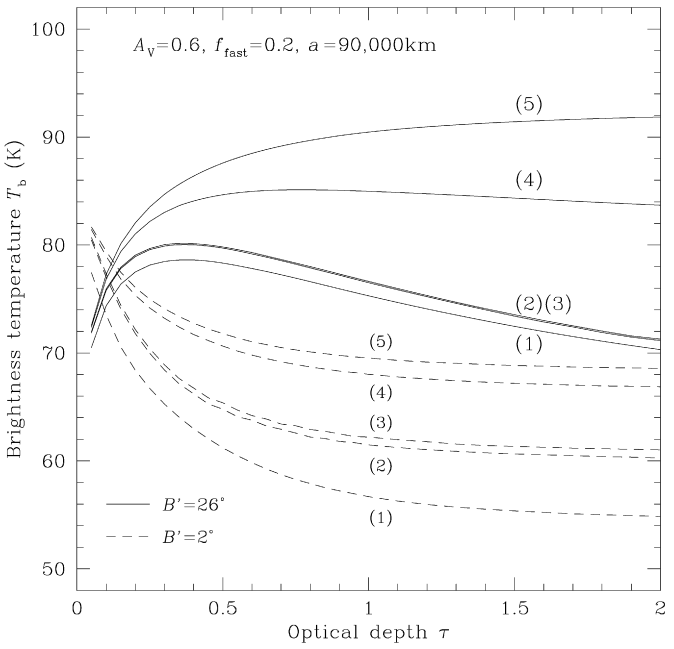

Fig. 13. Effect of different heat sources for various optical depths. The number next to each line indicates contributions from different heat sources in a similar manner as in Fig. 12.

only, while the curves with (2), (3), (4), and (5) correspond to the cases with two ($F_{\mathrm{Sun,V}}+F_{\mathrm{Sat,IR}}$), three ($F_{\mathrm{Sun,V}}+F_{\mathrm{Sat,IR}}+F_{\mathrm{Sat,V}}$), four ($F_{\mathrm{Sun,V}}+F_{\mathrm{Sat,IR}}+F_{\mathrm{Sat,V}}+F_{\mathrm{Mut,IR}}$), and all five ($F_{\mathrm{Sun,V}}+F_{\mathrm{Sat,IR}}+F_{\mathrm{Sat,V}}+F_{\mathrm{Mut,IR}}+F_{\mathrm{Sca,V}}$) heat sources. The contribution from Saturn is relatively more important for small B' and a. For optically thick rings, like the A and B rings, the contributions from the mutual heating and the multiple scattering of visible light are large, in particular, for large $|B'|$. These contributions significantly enhance the increase of T_b with $|B'|$. The multiple scattering effect is ignored in Kawata (1983), but it is clearly important for the A and B rings.

Fig. 13 shows the dependence of T_b on τ for the case with various heat sources. If the elevation angles of the Sun and observer are small ($B'=B=2°$), T_b always decreases with decreasing τ due to the effect of mutual shadowing and vertical heat transport. However, the contributions from $F_{\mathrm{Sca,V}}$ and $F_{\mathrm{Mut,IR}}$ increase with increasing τ. Also, in contrast to the solar illumination, the illumination from Saturn always takes place from a large effective elevation angle, so that it is not severely attenuated even for large τ. When the elevation angles of the Sun and observer are large ($B=26°$), T_b increases with increasing τ at small τ because the geometric filling factor increases with increasing τ. At larger τ, T_b starts to decreases with τ if we ignore mutual heating and multiple scattering, due to the effects of mutual shadowing and vertical heat transport as in the case of small B'. If we take both the mutual heating and the multiple scattering into account, however, T_b increases with τ.

The contributions from various heat sources were shown in a secondary way in Figs. 12 and 13 through their effect on T_b. Figs. 14–16 directly show the energy flux from various heat sources received by a particle as a function of the vertical coordinate z. For the case of slow rotators, each energy flux varies with the normal direction of the particle facet, and the fluxes received at the subsolar point and anti-subsolar point are chosen as extreme examples. As can be expected, the direct solar illumination is usually the most dominant heat source at large z, except for the anti-subsolar point for the slow rotators. The direct solar illumination rapidly attenuates with decreasing z, in particular, for large τ or small B'.

The second most important flux is the mutual heating, or in the case of small τ and a, the thermal emission from Saturn. In Figs. 14–16, we show the sum of the thermal emission from Saturn and the reflected sunlight by Saturn, but the former is one order of magnitude larger than the latter at the west ansa. Although the precise method to obtain the energy flux received by a ring particle is described in Section 2, let us roughly estimate the thermal fluxes from Saturn and surrounding particles in order to understand the dependence of these fluxes on the distance from Saturn and the optical depth. The thermal flux received by a particle is represented by the product of the solid angle of the heat source normalized by 4π, the thermal flux emitted by the heat source $\sigma_{\mathrm{SB}}T^4$, and the spin function Φ (see Eqs. (39) and (40)). The solid angle of Saturn, Ω_S, seen from a particle at a is given by

$$\frac{\Omega_S}{4\pi}=\frac{1}{2}\left(1-\sqrt{1-\left(\frac{r_{S,eq}}{a}\right)^2}\right)\frac{1-\varepsilon_S}{\sqrt{1-(r_{S,eq}/a)^2[1-(1-\varepsilon_S)^2]}}. \quad (48)$$

Note that $\Omega_S=2\pi$ at $a=r_{S,eq}$ and $\Omega_S=\pi r_{S,eq}^2(1-\varepsilon_S)$ for $a\gg r_{S,eq}$. The geometrical filling factor of surrounding particles seen from a particle at ξ toward a certain direction is given by $1-\exp(-\xi/\mu)$ for the upper layers and $1-\exp(-(\tau-\xi)/|\mu|)$ for the lower layers. Then, the solid angle of surrounding particles $\Omega_R(\xi)$ seen from the particle is given by averaging the geometrical factor over μ as

$$\begin{aligned}\frac{\Omega_R(\xi)}{4\pi}&=\frac{1}{2}\int_{-1}^{0}\left[1-\exp\left(-\frac{\tau-\xi}{\mu}\right)\right]d\mu\\&\quad+\frac{1}{2}\int_{0}^{1}\left[1-\exp\left(-\frac{\xi}{\mu}\right)\right]d\mu\\&=1+\frac{1}{2}\big[(\tau-\xi)E_1(\tau-\xi)\\&\quad+\xi E_1(\xi)-e^{-(\tau-\xi)}-e^{-\xi}\big],\end{aligned} \quad (49)$$

where $E_1(\xi)$ is the first order exponential integral.

For the case of the C ring ($a=80{,}000$ km and $\tau=0.08$), $\Omega_S/(4\pi)=0.15$ and $\Omega_R/(4\pi)=0.17$ and 0.19 at $\xi=0$ and $\tau/2$. Since the surface temperature of Saturn T_S (= 95 K) and the vertically averaged temperature of surrounding particles $\langle T_R\rangle\sim 90$ K (see Fig. 9) are similar as well as the solid angles, both fluxes to a fast rotator ($\Phi=1$) take similar values. The flux $\sigma_{\mathrm{SB}}T_S^4\Omega_S/(4\pi)$ is estimated to be 0.7 W m^{-2} with $T_S=95$ K and $\Omega_S/(4\pi)=0.15$ for the case of fast rotators and is consistent with our detailed numerical calculations. For slow rotators, we need to take the factor due to the spin function into account (i.e. the direction of the heat sources seen from a facet on a particle). At large z, the mutual heating flux of slow rotators at the subsolar/anti-subsolar point is usually smaller/larger than that for fast rotators, since the solid angle of surrounding particles seen from the facet at the subsolar/anti-subsolar point is relatively smaller/larger (the solid angle is normalized by 2π for a facet on the slow rotator).

For the A and B rings, the flux from Saturn becomes smaller as its solid angle is smaller. On the other hand, the mutual heating flux is significantly larger than that for the C ring. At sufficiently large τ, $\Omega_R/(4\pi)=0.5$ and 1 at $\xi=0$ and $\tau/2$. In this case, if the vertically averaged temperature of surrounding particles is as warm as the particle temperature at certain ξ, the contribution of the mutual heating at ξ exceeds, at least, half of the total flux for fast rotators. Indeed, this situation occurs for the B ring at $B'=26°$ (see also Fig. 9). For $B'=2°$, the contribution of the mutual heating is much lower than that for $B'=26°$, because of the low $\langle T_R\rangle$.

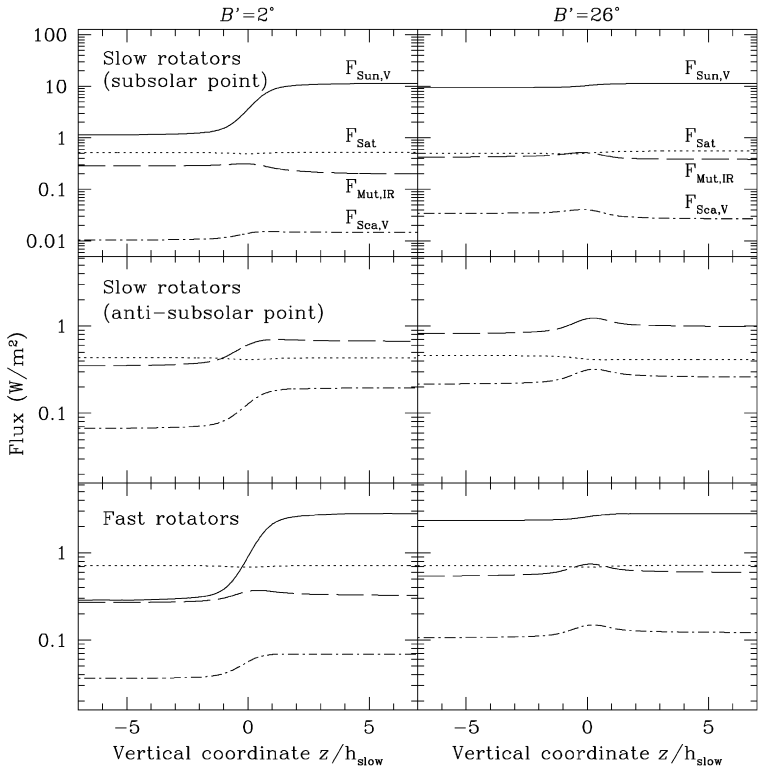

Fig. 14. Energy fluxes from different heat sources received by a particle at the vertical location z for the C ring. The parameters are $\tau = 0.08$, $A_V = 0.3$, $a = 80{,}000$ km, and $f_{\rm fast} = 0.2$. The solar elevation angle B' is 2° for the left panels and 26° for the right panels. The cases for the subsolar point (top panel) and the anti-subsolar point (middle panel) for slow rotators, and the case of fast rotators (bottom panel) are shown. Only the vertical motion is taken into account at $\phi = 270°$ (the west ansa).

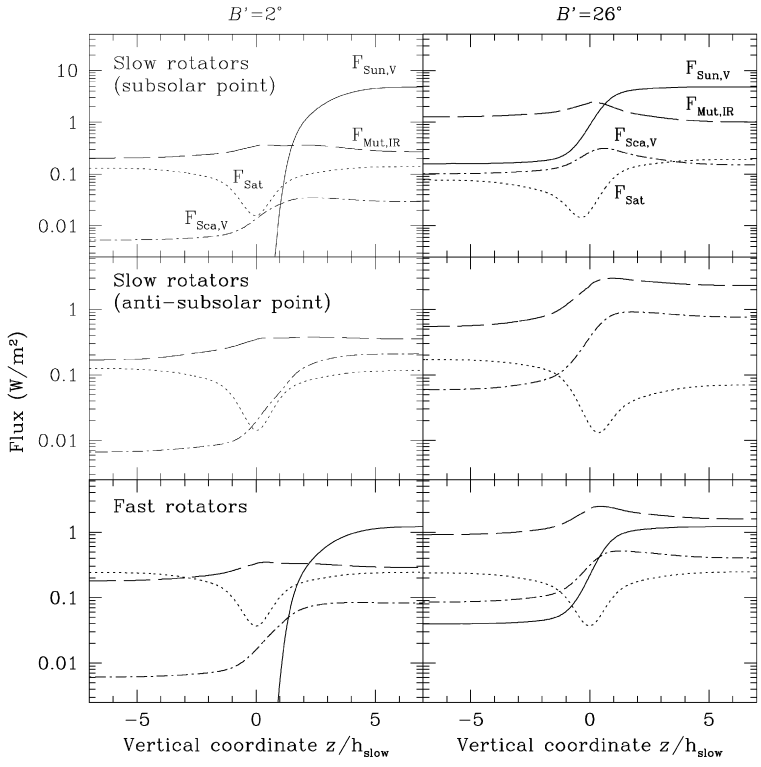

Fig. 15. Same as Fig. 14 but for the case of the B ring. The parameters are $\tau = 1.5$, $A_V = 0.7$, $a = 100{,}000$ km, and $f_{\rm fast} = 0.2$.

The scattered light is dominated by the first order scattered light which illuminates mainly the night-side hemispheres of particles. Therefore, its direct contribution is small at the subsolar point of slow rotators. However, since the night-side hemispheres of slow rotators are heated up by the scattered light, the effect of the mutual heating on the subsolar point increases. This is why the observed T_b is significantly enhanced by the scattered light in Figs. 12 and 13. For the case of fast rotators, the flux due to the

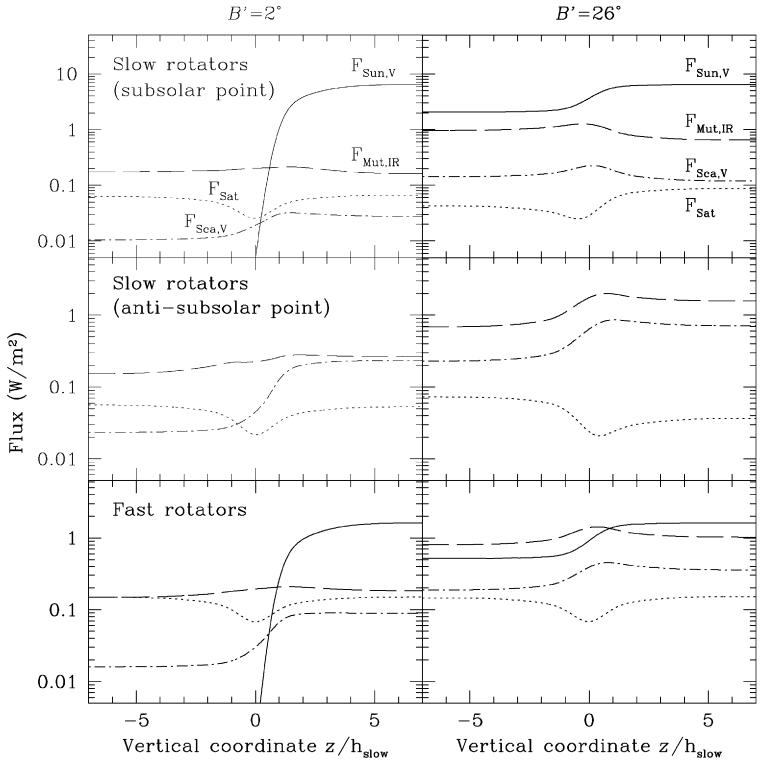

Fig. 16. Same as Fig. 14 but for the case of the A ring. The parameters are $\tau = 0.5$, $A_V = 0.6$, $a = 130{,}000$ km, and $f_{fast} = 0.2$.

first order scattered light can heat up entire surfaces by their fast spins. The mutual heating flux for fast rotators is approximately enhanced by a factor of $(F_{ext} + F_{Sca,V})/F_{ext}$ by the scattered light, where $F_{ext} = F_{Sun,V} + F_{Sat,V} + F_{Sat,IR}$.

Some discussion for the contribution of each heat source for a monolayer model can be found in Ferrari and Leyrat (2006).

3.4. Dependence on albedo, emissivity, and wavelength

If we extract the dependence of the fluxes on the albedo and emissivity, the energy balance equation at the particle surface (Eq. (37)) can be approximately rewritten as

$$K\left.\frac{\partial T_p}{\partial r}\right|_{r=R} = -\epsilon\left(1-\frac{\Omega_R}{4\pi}\right)\sigma_{SB}T_p^4 + (1-A_V)(c_{Sun,V} + c_{Sat,V} + A_V c_{Sca,V}) + F_{Sat,IR}, \quad (50)$$

where $c_{Sun,V}$, $c_{Sat,V}$, $c_{Sca,V}$ are factors for the fluxes other than the albedo (e.g., $F_{Sun,V} = (1-A_V)c_{Sun,V}$). In the above, we ignore the scattered light larger than the first order and the temperature of surrounding particles is assumed to be the same as the particle in question (thus, here Ω_R is interpreted as the effective solid angle of surrounding particles with the same temperature). Since the direct solar illumination is, in principle, the dominant heat source, T_p and T_b increase with decreasing A_V (Fig. 17). In the case of $A_V = 1.0$, the particle temperature is determined by Saturn's infrared flux and T_b decreases with increasing B', as a larger fraction of cold particles near the midplane are visible. Except for the case of $A_V \sim 1.0$, T_p monotonically increases with increasing B' and the dependence of T_b on B' are similar for different A_V's.

The reduction of ϵ has an effect similar to the decrease of A_V. If $(1-A_V)/\epsilon$ takes the same value, T_p, determined by the direct solar illumination only, takes the same value as well for static particles. For moving particle, T_p slightly deviates for cases of different values of ϵ even with the same $(1-A_V)/\epsilon$, because the thermal conduction term is relatively more important for smaller ϵ.

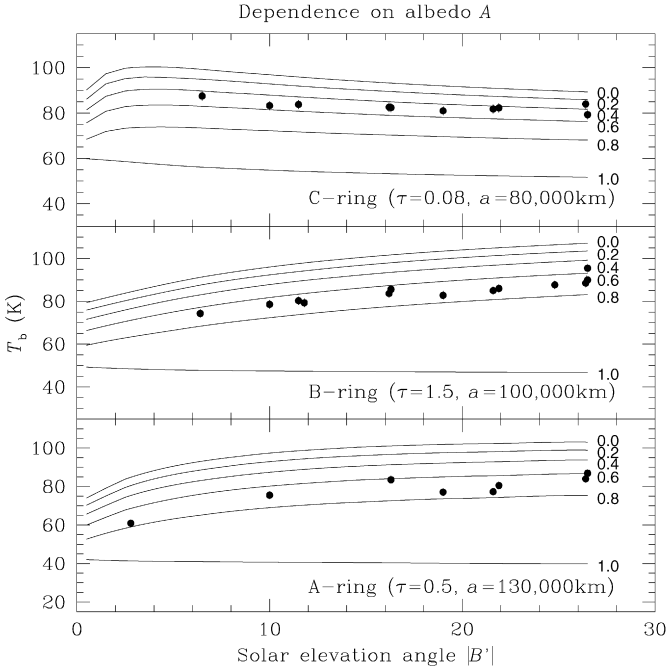

Fig. 17. Dependence of brightness temperature on albedo A_V (the number next to each line). Here $\Gamma = 6\ \mathrm{J\,m^{-2}\,K^{-1}\,s^{-1/2}}$ and $f_{fast} = 0.2$.

The deviation of the temperature due to this effect is very small though. Fig. 18 shows T_b and T_{eff} for the case of $\epsilon = 0.5$ and 1.0 and both cases take the same $(1-A_V)/\epsilon$. All the heat sources are included in the simulations. For the case of $\epsilon = 1.0$, T_b at 20 μm and T_{eff} fitted from the spectrum between 25–100 μm almost coincide if the geometric filling factor $\beta_f = 1 - \exp(-\tau/|\sin B'|)$ is nearly unity (for the case of the B-ring two lines are indistinguishable for all B' due to large τ). For $\epsilon = 0.5$, T_{eff} is larger than that

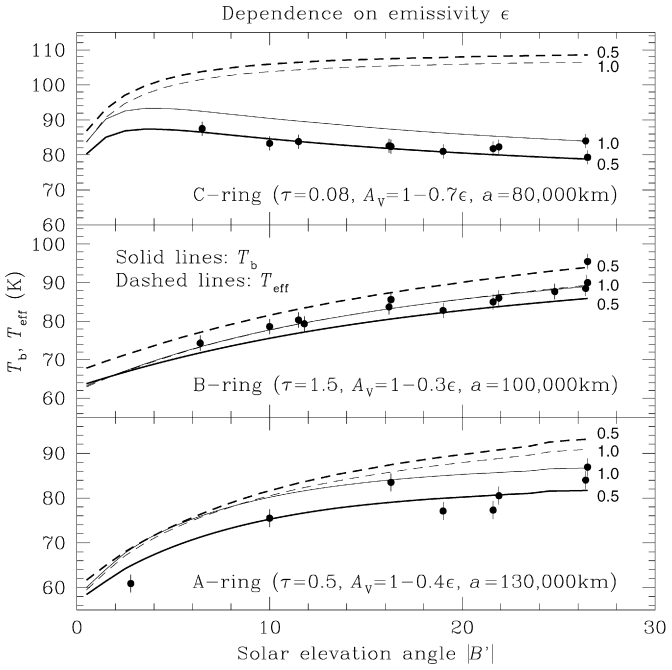

Fig. 18. Dependence of brightness temperature (solid lines) and effective temperature (dashed lines) on emissivity. Two different cases of $\epsilon = 0.5$ and 1.0 (the number next to each line) with a fixed $(1 - A_V)/\epsilon$ are shown. Here $\Gamma = 6\ \mathrm{J\,m^{-2}\,K^{-1}\,s^{-1/2}}$ and $f_{\mathrm{fast}} = 0.2$.

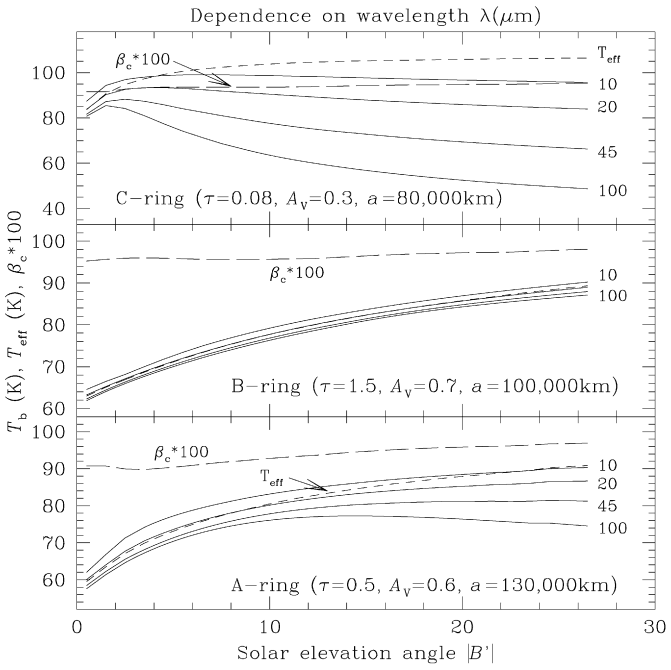

Fig. 19. Dependence of brightness temperatures (solid lines) on wavelength. The number next to each line indicates the wavelength in units of μm. The effective temperature (short-dashed line) and the scaling factor β_c (long-dashed line) multiplied by a factor 100 are also shown. Here $\Gamma = 6\ \mathrm{J\,m^{-2}\,K^{-1}\,s^{-1/2}}$ and $f_{\mathrm{fast}} = 0.2$.

for $\epsilon = 1.0$, whereas T_b is lower than that for $\epsilon = 1.0$. This is explained as follows. The dependence of T_{eff} and T_b on A_V and ϵ are given as (see Eq. (50) and Section 2.3.3):

$$T_{\mathrm{eff}}^4 \sim T_p^4 \propto \left(\frac{1 - A_V}{\epsilon}\right)(c_{\mathrm{Sun,V}} + c_{\mathrm{sat,V}} + A_V c_{\mathrm{Sca,V}}) + \frac{F_{\mathrm{Sat,IR}}}{\epsilon}, \quad (51)$$

$$T_b^\gamma \sim \beta_f \epsilon T_p^\gamma. \quad (52)$$

If $(1 - A_V)/\epsilon$ takes the same value, the thermal flux from Saturn and the flux due to the multiple scattering relatively increases with decreasing ϵ: the former is important for the C ring and the latter for the B and A rings. Therefore, T_p itself is higher for smaller ϵ with a fixed $(1 - A_V)/\epsilon$. On the other hand, T_b is proportional to $\epsilon^{1/\gamma}$ if T_p is constant. Thus, T_b decreases with decreasing ϵ, even though T_p slightly increases. It is found from Eqs. (51) and (52) that if $(1 - A_V)/\epsilon^{1-4/\gamma}$ takes the same value, T_b also takes similar values to first order.

The dependence of T_b on the wavelength λ is shown in Fig. 19. With increasing λ, T_b decreases, and this trend is stronger for optically thinner rings. This is explained by the effect of the geometric filling factor, β_f. Equation (52) suggests that $T_b \sim \beta_f^{1/\gamma} T_p$. Since γ decreases with increasing λ (Eq. (30)), the decrease of T_b due to the effect of β_f is larger for larger λ. Even without the effect of β_f, T_b slightly increases with decreasing λ, since larger weights are put on particles with high T_p in the integrating procedure to obtain the observed intensity (Eq. (28); $S_{\mathrm{IR},\lambda} \propto T_p^\gamma$). This causes weak λ-dependence of T_b even for the B ring, where $\beta_f \simeq 1$ for any $|B'|$.

We also plot T_{eff} and β_c in Fig. 19. As we explained in Section 3.1, T_{eff} monotonically increases with increasing B'. We find that β_c usually takes values between 0.9 and 1.0 and gradually increases with increasing B'. The β_c factor represents the temperature variation of particles and facets seen from the observer: β_c increases to unity as the variation becomes smaller. The temperature variation in the vertical direction is large at small B'. With increasing B', the temperature variation becomes smaller as the direct solar illumination reaches deeply and β_c approaches close to unity for all the rings.

4. Fitting to observed temperatures

As we have shown in Section 3, the main parameters controlling the brightness temperature of a ring are the albedo for visible light A_V, the fraction of fast rotators f_{fast}, the thermal inertia Γ, the optical depth τ, the distance from the Saturn center a, emissivity ϵ, and the ratio of the scale height of the fast rotators to that for the slow rotators h_r. We assume that $\epsilon = 1$ and $h_r = 3$: for both parameters, deviations from actual values are expected to be small as $\epsilon \sim 0.9$ (Altobelli et al., 2008) and $h_r \sim 3$ from dynamical simulations (e.g., Morishima and Salo, 2006). The optical depth τ is well determined by previous observations, such as those by the Voyager photopolarimeter subsystem (PPS; Esposito et al., 1983) as a function of a except for dense parts ($\tau > 2.0$). In fact, in rings with wakes, the (normal) optical depth τ is a function of the elevation angle of the observer (Colwell et al., 2006, 2007), as predicted by Salo et al. (2004). In the present paper, however, we ignore the effect of wakes, as mentioned in Section 2.1, and adopt the optical depths obtained by the Voyager observations as nominal values.

Then, we focus on the following three unknown parameters, f_{fast}, A_V, and Γ. Unfortunately, we cannot determine them accurately when using only data from Earth-based observations because there is a tradeoff relation in these parameters. For example, with increasing both f_{fast} and A_V, observed temperatures similarly decrease. Therefore, in the present paper, we attempt to obtain possible combinations of f_{fast}, A_V, and Γ which satisfy the observational data. In order to save the computational time, we consider only three cases of $\Gamma = 2$, 6, and 20 $\mathrm{J\,m^{-2}\,K^{-1}\,s^{-1/2}}$. Note that the lower and upper limits obtained by previous works are about $\Gamma = 2$ and 30 $\mathrm{J\,m^{-2}\,K^{-1}\,s^{-1/2}}$, respectively (Froidevaux et al., 1981; Ferrari et al., 2005; Leyrat et al., 2008), and the difference between results for 20 and 30 $\mathrm{J\,m^{-2}\,K^{-1}\,s^{-1/2}}$ is expected to be small.

4.1. Infrared data

The observational data used for the fit are tabulated in Table 1. Except for the Pioneer data at ∼45 μm, the data at ∼20 μm are

chosen, since there are a largest number of observations at this wavelength as compared with those in other wavelengths. All the data are normalized to Saturn's disk center brightness temperature of $T_{\rm disk,st} = 92$ K at $a_\odot = 9.25$ AU, following Nolt et al. (1978) and Froidevaux (1981). Note that the brightness temperature is not necessarily the same as the effective temperature $T_S = 95$ K. The standard disk temperature $T_{\rm disk,st}(a_\odot)$ at $a_\odot$ according to the effective temperature relation is given as

$$T_{\rm disk,st}(a_\odot) = \left[0.5\left(\frac{9.25\ \text{AU}}{a_\odot}\right)^2 + 0.5\right]^{1/4} T_{\rm disk,st}(9.25\ \text{AU}), \qquad (53)$$

where equal solar and internal energy sources are assumed. Using $T_{\rm disk,st}(a_\odot)$, the brightness temperature of a ring at $a_\odot$ is normalized as

$$I_{B,\lambda}\big(T_b(a_\odot),\lambda\big) = I_{B,\lambda}\big(T_{b,\rm obs}(a_\odot),\lambda\big)\frac{I_{B,\lambda}(T_{\rm disk,st}(a_\odot),\lambda)}{I_{B,\lambda}(T_{\rm disk}(a_\odot),\lambda)}, \qquad (54)$$

where $I_{B,\lambda}(T,\lambda)$ is the Planck function and $T_{b,\rm obs}$ is the actual observed brightness temperature before the normalization. Then, $T_b(a_\odot)$ is normalized to 9.25 AU, according to the expected dependence on $a_\odot$ as

$$T_b(9.25\ \text{AU}) = T_b(a_\odot)\left(\frac{a}{9.25\ \text{AU}}\right)^{1/2}. \qquad (55)$$

The brightness temperatures after the normalization are indicated in parentheses next to the actual observed brightness temperatures before the normalization in Table 1. After the normalization, we simply assume the error bar size to be 2 K for all the data after Froidevaux (1981). Without the above normalization, the scatter of the raw data is too large to constrain physical parameters accurately in data fitting.

The observed brightness temperatures are already plotted in previous figures (filled circles) and Fig. 18 is a good example to explain. For the A and B rings, T_b monotonically increases with increasing $|B'|$ (the thermal tilt effect). On the other hand, T_b for the C ring decreases with increasing $|B'|$ except for very small $|B'|$. This is because of the small geometric filling factor of the C ring. It is expected, however, that $T_{\rm eff}$ of the C ring monotonically increases with increasing $|B'|$ as well as those for the A and B rings.

There are some other observations not listed in Table 1. In particular, data from Pioneer (Froidevaux and Ingersoll, 1980) and Voyager (Hanel et al., 1981, 1982) are very attractive to analyze, as these were obtained at small $|B'|$. Note that there are very few data from Earth-based observations at small $|B'|$, perhaps because small opening of rings makes accurate observations difficult. However, we avoided the data obtained at observational geometries which are very different from the Earth based observations. Interpretations of these data are more complicated. One lit-side data for the A ring, which we take from the Pioneer observation, has a nearly same geometry of the Earth based observation (see Froidevaux, 1981). We also use the unlit side temperature of the A ring. The effective temperature is used only for this case. Since the elevation angle of the spacecraft was really small for the unlit side observation ($|B| < 1°$), it mostly observed vertically extended fast rotators. Therefore, the phase angle dependence is expected to be very small.

4.2. Results

Figs. 20–22 show the albedo obtained by the χ-square fitting as a function of the fraction of fast rotators $f_{\rm fast}$ for three different values of Γ (the upper panels). In the lower panels, the standard deviation for the fitting to the observed temperatures is shown. In all the rings, the fitted albedo decreases with increasing $f_{\rm fast}$ and Γ. The temperatures of the ring particles at large z, which

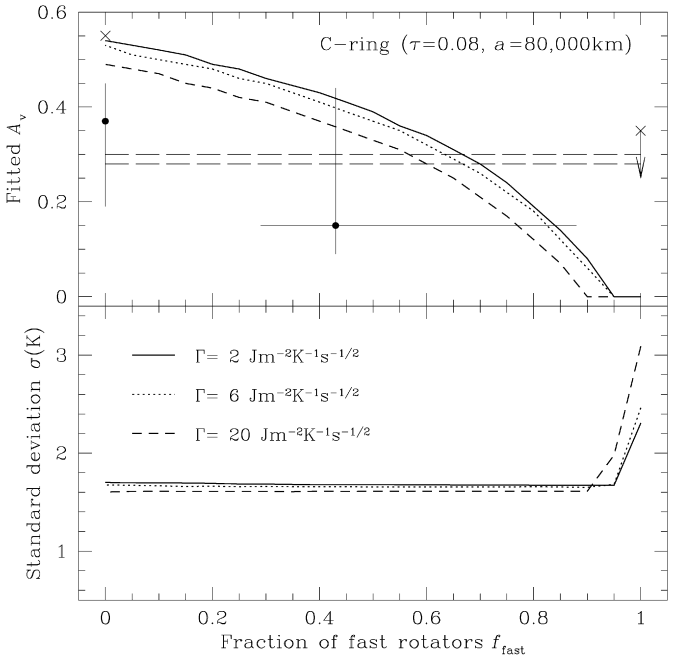

Fig. 20. Upper panel: Fitted albedo in visible light as a function of the fraction of fast rotators $f_{\rm fast}$ for the case of the C ring. The results for three different Γ's are shown. The error bar size is 0.02–0.04 (not shown). The region between two horizontal dashed lines indicate the range of the albedo obtained from optical and near-infrared observations (see Section 5.1). The dots with error bars are the values of A_V and $f_{\rm fast}$ estimated by Leyrat et al. (2008). They use a data set by Voyager IRIS and adopt the mono-size ($f_{\rm fast} = 0$) and bimodal size approximations. The cross marks are the values of A_V estimated in Froidevaux (1981) for the cases of $f_{\rm fast} = 0$ and 1. Lower panel: Standard deviation in the χ-square fitting to the observed temperatures.

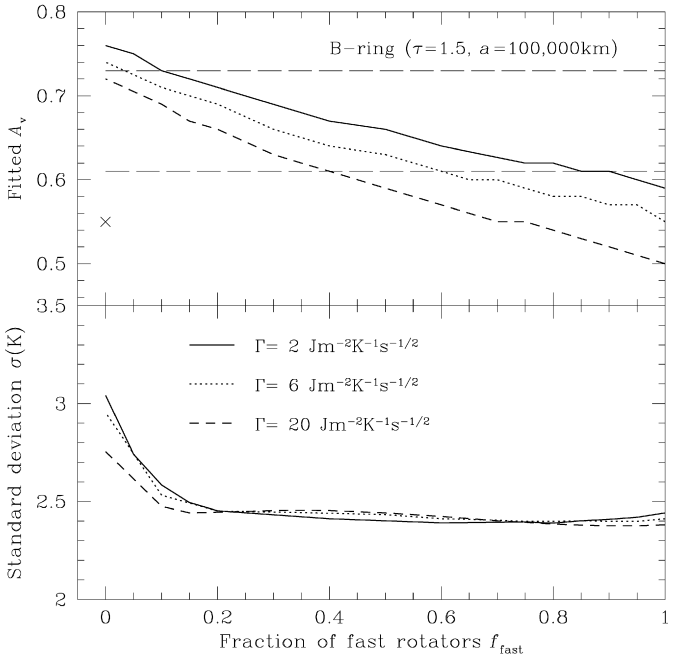

Fig. 21. Same as Fig. 20, but for the case of the B ring. The error bar size is 0.01–0.03. The value for $f_{\rm fast} = 1$ estimated in Froidevaux (1981) is less than 0.05 (outside of the range of this figure).

are primarily observed from the Earth, decreases due to vertical motion of ring particles and the eclipse cooling, and both effects are more enhanced with larger Γ.

If all the ring particles are slow rotators ($f_{\rm fast} = 0$), the estimated albedo A_V is 0.52 ± 0.05, 0.74 ± 0.03, and 0.74 ± 0.06 for

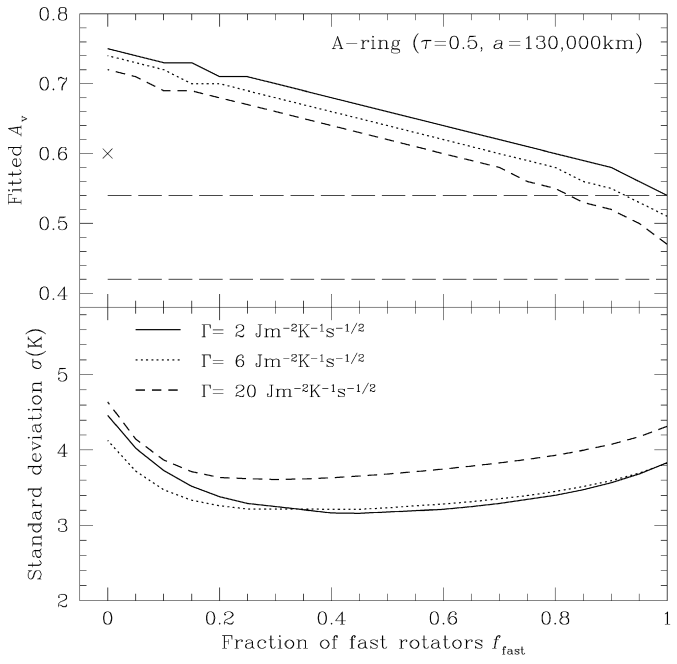

Fig. 22. Same as Fig. 20, but for the case of the A ring. The error bar size is 0.02–0.05. The value for $f_{\rm fast} = 1$ estimated in Froidevaux (1981) is less than 0.05 (outside of the range of this figure).

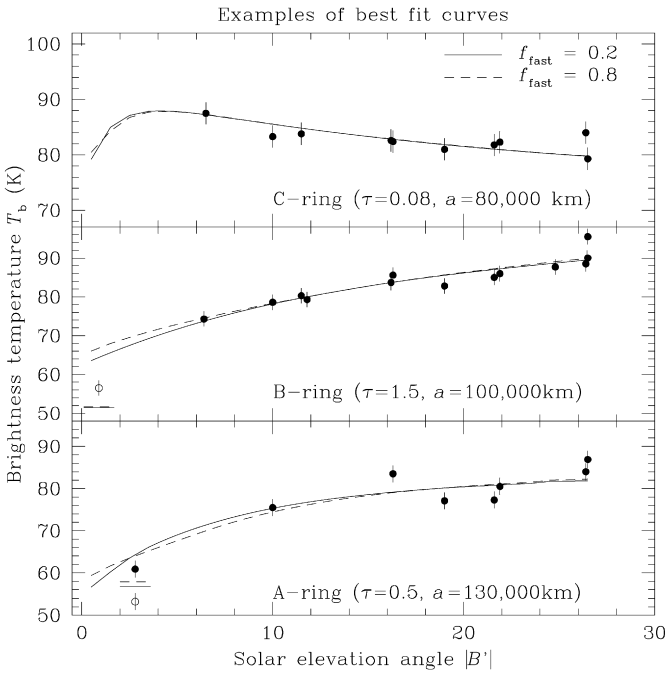

Fig. 23. Examples of best-fit curves. Two cases of $f_{\rm fast} = 0.2$ (solid curve) and 0.8 (dashes curve) are shown. The thermal inertia is $\Gamma = 6\ {\rm J\,m^{-2}\,K^{-1}\,s^{-1/2}}$ and the values of the albedo shown in Figs. 20–22 are adopted. Horizontal lines are unlit side temperatures from simulations while open circles are from observations (Table 1).

the C, B, and A ring, respectively. On the other hand, if all the ring particles are fast rotators ($f_{\rm fast} = 1$), the estimated albedo is 0, 0.55 ± 0.07, and 0.51 ± 0.07 for the C, B, and A ring. Here, the error size comes from the fitting error and the uncertainty of Γ between 2 and 20 $\rm J\,m^{-2}\,K^{-1}\,s^{-1/2}$. Since the actual value of $f_{\rm fast}$ is expected to be somewhere between 0 and 1, the actual albedo would be somewhere between the above estimated values.

Since the standard deviation σ takes similar minimum values for a wide range of $f_{\rm fast}$, we cannot really clarify which $f_{\rm fast}$ is most probable. However, in some ranges of $f_{\rm fast}$, σ takes larger values, so these ranges are likely to be excluded. For the case of the C ring, some fraction of slow rotators is necessary ($f_{\rm fast} \leqslant 0.9$), otherwise the brightness temperature can not be as warm as observed even for $A_{\rm V} = 0$. For the case of the B ring, some fraction of fast rotators is necessary ($f_{\rm fast} \geqslant 0.1$–$0.2$) in order to reproduce the steep dependence of $T_{\rm b}$ on B'. Similarly to the B ring, intermediate values of $f_{\rm fast}$ are preferred for the A ring. The standard deviation for the A ring with $\Gamma = 20\ {\rm J\,m^{-2}\,K^{-1}\,s^{-1/2}}$ is larger than the cases with smaller Γ. This comes from the unlit side temperature which is much warmer than the observed temperature for large Γ (see below).

Fig. 23 shows the best-fit brightness temperature for the two examples with $f_{\rm fast} = 0.2$ and 0.8. The thermal inertia adopted is $6\ {\rm J\,m^{-2}\,K^{-1}\,s^{-1/2}}$ and the values of the albedos in Figs. 20–22 are used. As expected from similar values of σ shown in Figs. 20–22, the lines of two cases of $f_{\rm fast}$ are almost indistinguishable. For the case of the B and A rings, we also plot the unlit side temperatures from our simulations and observations (Table 1).

For the case of the B ring, the unlit temperature from our simulation (∼51 K) is always smaller than the observed value (∼56 K). Since the heat transport is efficiently prevented in the bouncing model and the direct solar illumination does not reach to the unlit side at very small B', the unlit temperatures from our simulations is mostly determined by the thermal flux from Saturn. The higher observed temperature probably indicates that the solar illumination leaks to the unlit side through optically thinner parts of the ring. Note that Saturn's disk temperature for this observation is not shown in Tokunaga et al. (1980) so the normalization to the disk temperature is not done. The observed value might be smaller after the normalization.

For the case of the A ring, the unlit side temperature and the lit side temperature at low B' from our best fit curve $\Gamma = 6\ {\rm J\,m^{-2}\,K^{-1}\,s^{-1/2}}$ are slightly higher than the observed value by Pioneer (∼53 K and ∼61 K, respectively). The temperatures of the both sides strongly depend on Γ, when B' is small (note that we apply the sinusoidal vertical motion for the A ring). With increasing Γ (i.e. more efficient vertical heat transport) the lit/unlit side temperature decreases/increases. In particular, the increase of the unlit side temperature is large. This makes the slightly larger standard deviation (and error bar size) in Fig. 22 for $\Gamma = 20\ {\rm J\,m^{-2}\,K^{-1}\,s^{-1/2}}$ than those for smaller Γ's. The number of the data is not sufficient for the A ring and the standard deviation is large, as compared with those for the B and C rings. Further observations with wide range of B' are necessary for more accurate determination of physical parameters.

5. Constraints from other observations and models

5.1. Albedo from optical and near-infrared observations

The albedo in optical and near-infrared wavelengths strongly depends on wavelength. The albedo $A_{\rm V}$ we used in this paper is the one averaged over wavelength (Eq. (18)). We here calculate the value of $A_{\rm V}$ using A_λ directly obtained from optical and near-infrared observations. For the optical observations, we use A_λ in five different bands (338, 451, 568, 650, and 862 nm) from Fig. 3 of Porco et al. (2005). We linearly interpolate the A_λ values between different bands. For $\lambda < 338$ nm, we linearly extrapolate using $A_{\lambda=338\ {\rm nm}}$ and $A_{\lambda=451\ {\rm nm}}$ and set $A_\lambda = 0$ if $A_\lambda < 0$. For the near-infrared observations, we use the spectra shown in Figs. 3 and 5 of Poulet et al. (2003), provided that their spectra $(I/F)(\lambda)$ are proportional to A_λ (i.e. the single scattering is assumed to be dominant). We assume that A_λ is constant between 862 nm

and 1000 nm and $(I/F)(\lambda)$ at 1000 nm is scaled to the value of $A_{\lambda=862\ \mathrm{nm}}$ from Porco et al. (2005). The integration over wavelength is done up to 5 μm. The solar intensity is negligible for further longer wavelengths.

The averaged value is $A_V = 0.29 \pm 0.01$, 0.67 ± 0.06, and 0.48 ± 0.06 for the C, B, and A rings, respectively. The errors come from variation due to different locations and from the rough interpolation of the albedo over wavelengths (0.01 for the latter). We excluded the albedos for the outer C ring and the innermost B ring, as these values are very different from those for most other parts of the C and B rings, respectively. For the C ring, we used only one set of albedos at 81,000 km (see Figs. 3 and S2b of Porco et al., 2005).

The evaluated ranges of A_V are plotted in Figs. 20–22. Provided that the probable range of the thermal inertia Γ is between 2 and 20 $\mathrm{J\,m^{-2}\,K^{-1}\,s^{-1/2}}$, the possible range of the fraction of fast rotators, f_{fast}, is 0.5–0.75, 0–1.0, and 0.7–1.0 for the C, B, and A rings, respectively. We took into account the error size of the albedo we estimated. Since the value of f_{fast} for the B ring sensitively depends on A_V and Γ, f_{fast} cannot be constrained as long as there are some uncertainties in A_V and Γ. Nevertheless, since the standard deviation in Fig. 21 suggests that some fraction of fast rotators is necessary for the B ring, at least some fraction of fast rotators is expected for all the rings.

5.2. Relation between the thermal inertia and the fraction of fast rotators

We have treated the thermal inertia Γ and the fraction of fast rotators f_{fast} as independent parameters so far. However, they are not independent of each other if the size distribution of ring particles and their spin frequencies are given. Or if Γ and f_{fast} are evaluated independently, the size and spin distributions of ring particles can be constrained. In the following, we derive an approximate relation between Γ and f_{fast}.

When the spin period of a ring particle τ_{spin} is sufficiently shorter/longer than the thermal relaxation time τ_{rel} (Eq. (44)), the particle is assumed to be a fast/slow rotator. In actual rings, the spin distribution is not bimodal but continuous. Dynamical simulations suggest that the spin period of the largest particle (with size R_{max}) is about the orbital period, τ_{orb}, while the spin period is roughly proportional to the particle size for particles with an extended size distribution (Salo, 1987; Ohtsuki, 2005, 2006b; Morishima and Salo, 2006):

$$\tau_{\mathrm{spin}}(R) = \tau_{\mathrm{orb}} \frac{R}{R_{\mathrm{max}}}. \tag{56}$$

In order to relate the actual continuous size distribution with the bimodal size distribution, we approximately regard particles with spin period shorter/longer than the thermal relaxation time to be fast/slow rotators. The critical size, R_{crit}, of a particle whose spin period is equal to the thermal relaxation time ($\tau_{\mathrm{spin}}(R_{\mathrm{crit}}) = \tau_{\mathrm{rel}}$) is given by

$$\frac{R_{\mathrm{crit}}}{R_{\mathrm{max}}} = \left(\frac{\Gamma}{\epsilon \sigma_{\mathrm{SB}} T_{\mathrm{p}}^3} \right)^2 \frac{1}{2\pi \tau_{\mathrm{orb}}}. \tag{57}$$

Assuming that the particle number density $n(R)$ per unit size is given by a power-law distribution as $n(R) \propto R^{-q} (R_{\mathrm{min}} \leqslant R \leqslant R_{\mathrm{max}})$, where R_{min} is the minimum size of particles, the fraction of fast spinning particles is given as

$$f_{\mathrm{fast}} = \frac{\int_{R_{\mathrm{min}}}^{R_{\mathrm{crit}}} n(R) R^2\, dR}{\int_{R_{\mathrm{min}}}^{R_{\mathrm{max}}} n(R) R^2\, dR} = \frac{(R_{\mathrm{crit}}/R_{\mathrm{max}})^{3-q} - (R_{\mathrm{min}}/R_{\mathrm{max}})^{3-q}}{1 - (R_{\mathrm{min}}/R_{\mathrm{max}})^{3-q}}. \tag{58}$$

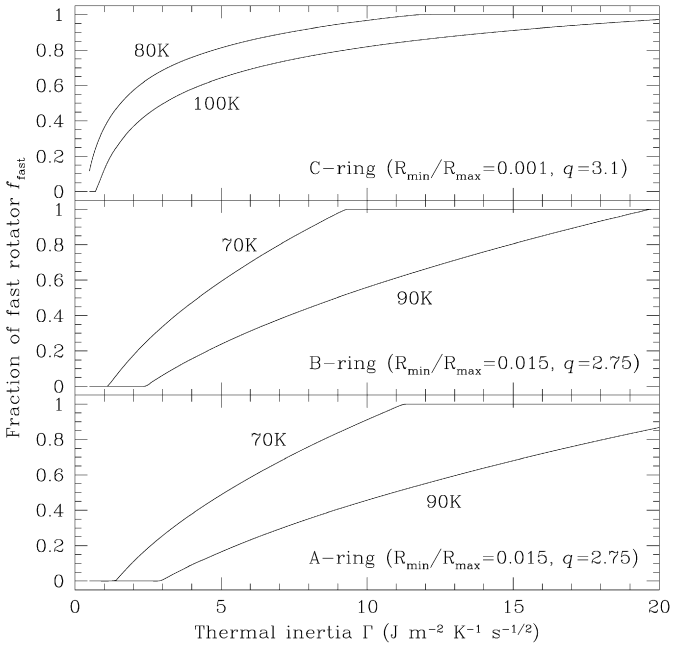

Fig. 24. Fraction of fast rotators as a function of thermal inertia with given physical temperatures (Eqs. (57) and (58)). The size distribution ($R_{\mathrm{min}}/R_{\mathrm{max}}$ and q) is from French and Nicholson (2000).

Equations (57) and (58) indicate that f_{fast} increases with increasing Γ and deceasing T_{p} and τ_{orb}, for given $R_{\mathrm{min}}/R_{\mathrm{max}}$ and q.

Using the values of $R_{\mathrm{min}}/R_{\mathrm{max}}$ and q estimated in French and Nicholson (2000), we plot the value of f_{fast} as a function of Γ in Fig. 24. The probable range of T_{p} is chosen for each ring from Fig. 9. Since T_{p} decreases with decreasing B', f_{fast} is actually not constant but increases with decreasing B'. The data used for the fitting in Section 4 are, however, mainly obtained at somewhat large B', where variation of T_{p} with B' is not very large, and the dependence of T_{b} on f_{fast} is small at small B'. Therefore, the assumption of a constant f_{fast} is likely to be reasonable, although this may turn out to be incorrect if we have a sufficient number of accurate data at small B' in future.

If we assume the values of f_{fast} estimated in Section 5.1, Fig. 24 suggests $1.5\ \mathrm{J\,m^{-2}\,K^{-1}\,s^{-1/2}} < \Gamma < 8\ \mathrm{J\,m^{-2}\,K^{-1}\,s^{-1/2}}$ for the C ring and $\Gamma > 7\ \mathrm{J\,m^{-2}\,K^{-1}\,s^{-1/2}}$ for the A ring. Since the large Γ is not preferred from the unlit side temperature (Fig. 22), the value of Γ is restricted in a narrow range around $\sim 10\ \mathrm{J\,m^{-2}\,K^{-1}\,s^{-1/2}}$. These values of Γ for the C and A rings are roughly consistent with previous observations ($2–30\ \mathrm{J\,m^{-2}\,K^{-1}\,s^{-1/2}}$), although our estimations of Γ here are quite indirect.

5.3. Comparison with monolayer models

Leyrat et al. (2008) applied their monolayer model developed in Ferrari and Leyrat (2006) to three different sets of mid-infrared observations for the C ring: two by Earth-based instruments (CAMIRAS and VISIR) and one by Voyager IRIS. For all the three sets, they applied the model with the mono-size approximation while they also applied the bimodal size approximation, similarly to ours, for the Voyager IRIS data. For the case of the mono-size approximation, their best-fit spin rate is about half of the synchronous rotation rate and the fitted albedo A_V is $0.25^{+0.08}_{-0.01}$, 0.24 ± 0.01, and $0.37^{+0.08}_{-0.18}$ for CAMIRAS, VISIR, and Voyager IRIS, respectively. They found that a better fit to the Voyager IRIS data can be obtained with a bimodal size approximation, in particular, at high phase angles. Their estimated fraction of fast rotator, f_{fast}, is $0.45^{+0.43}_{-0.16}$ while

the fitted albedo $A_V = 0.15^{+0.29}_{-0.06}$ is lower than that estimated in the mono-size approximation.

Their estimated parameters from the Voyager IRIS data are overplotted in Fig. 20. For the mono-size approximation, we set $f_{fast} = 0$ as their estimated spin rate is very low. We find that A_V from our model is larger than their estimates. For optically thin rings like the C ring, the difference between the monolayer and multilayer models is expected to be small. A part of the difference might be caused by the difference between non-spinning particles adopted in our model and actual slowly rotating particles in their model. The illuminated hemisphere for a non-spinning particle is effectively heated up while even rotation as slow as synchronous helps to cool the hemisphere. One needs to be careful for the meaning of f_{fast} for the bimodal size distribution, since the value depends on how the spin states of slow and fast rotators are defined. Since the observational geometries for the Earth-based observations and those for Voyager observations are very different, that might also cause some difference in A_V.

The values of the albedo estimated from their Earth-based observations are too low as compared with those obtained from our data fit. That is probably because they used the brightness temperatures without the normalization shown in Section 4.1. Since their observed brightness temperatures of rings and Saturn's disk are both high, the normalized brightness temperatures of the rings become much lower. This makes their estimated albedos lower than ours.

We also plot the values of A_V estimated by the monolayer model of Froidevaux (1981). He uses a set of data obtained in Earth-based observations similar to those used in this paper. For the case of the C ring, his estimated A_V's are similar to ours (he suggests $A_V < 0.35$ for $f_{fast} = 1$, but the lower limit is not clear). On the other hand, A_V's for the A and B rings from his estimation ($A_V < 0.05$ for $f_{fast} = 1$ for both the A and B rings; falling outside the range shown in Figs. 21 and 22) are lower than ours for both $f_{fast} = 0$ and 1. These deviations for the A and B rings are perhaps because of the larger contributions due to the multiple scattering and the mutual heating in our model. Another reason causing the difference may be new data not used in Froidevaux (1981), in particular, for the A ring, which has a small number of observational data. The recent observations by Ferrari et al. (2005) and Leyrat et al. (2008) ($|B'| \sim 20^\circ$) show relatively lower temperatures for the A and B rings than those in previous observations, after we apply the normalization in Section 4.1 (see Fig. 23).

6. Summary

We have developed a new model of the thermal infrared brightness of Saturn's rings based on classical radiative transfer, taking into account the vertical heterogeneity of spin frequencies of ring particles and the heat transport due to vertical and azimuthal motion of particles. In the present paper, we have applied our model to Earth-based observations. We have shown that the temperature increase with the solar elevation angle (the thermal tilt effect) is enhanced due to the vertical heat transport, the vertical heterogeneity of spins, and the mutual heating and multiple scattering of visible light for the A and B rings. We found that our model can well reproduce observed temperatures of Saturn's main rings without the vertical heterogeneity of the albedo in visible light, which was proposed in the previous multilayer model (Kawata, 1983).

Unfortunately, since there is degeneracy among the albedo, the fraction of fast rotators, and the thermal inertia, we can not precisely constrain these parameters. However, the range of the estimated albedo is limited to $0–0.52 \pm 0.05$, $0.55 \pm 0.07–0.74 \pm 0.03$, and $0.51 \pm 0.07–0.74 \pm 0.06$ for the C, B, and A rings, respectively. These lower and upper limits are obtained by assuming all ring particles are fast and slow rotators (non-spinning particles), respectively. The quoted errors of the limits correspond to values obtained for different values of the thermal inertia. For the C ring, some fraction of slow rotators is necessary ($f_{fast} \leqslant 0.9$) in order for the fitted albedo to be positive, whereas the A and B rings prefer non-zero fraction of fast rotators ($f_{fast} \geqslant 0.1–0.2$), which enhances the dependence of the observed brightness temperature on the solar elevation angle.

If we adopt the albedo values obtained by optical and near-infrared observations, the fraction of fast rotators is estimated to be 0.5–0.75, 0–1.0, and 0.7–1.0 for the C, B, and A rings, respectively. Further, if we assume the size distribution estimated from optical observations and spin distribution from dynamical simulations, the thermal inertia Γ is estimated to be smaller than $1.5\ \mathrm{J\,m^{-2}\,K^{-1}\,s^{-1/2}} < \Gamma < 8\ \mathrm{J\,m^{-2}\,K^{-1}\,s^{-1/2}}$ for the C ring and $\Gamma \sim 10\ \mathrm{J\,m^{-2}\,K^{-1}\,s^{-1/2}}$ for the A ring. However, these estimations for the fraction of fast rotators and the thermal inertia are quite indirect and more straitforward estimations using observed temperatures at various solar phase angles and azimuthal locations are necessary. Such measurements of ring temperatures are already obtained by the Cassini CIRS (e.g., Spilker et al., 2005, 2006), and we will apply our model to these observational data in our subsequent works.

Acknowledgments

We are grateful to L. Spilker and S. Pilorz for very helpful criticisms and advises as reviewers and N. Altobelli for fruitful discussions. Numerical simulations were conducted with the supercomputers Zbox1 and Zbox2 at University of Zurich. R.M. thanks Doug Potter and Joachim Stadel for helping him in using the computers. Part of this work was supported by the Academy of Finland and the Oulu University special research-unit grant. K.O. is grateful for the support by the Cassini project and NASA's Outer Planets Research Program.

References

Altobelli, N., Spilker, L., Pilorz, S., Brooks, S., Edgington, S., Wallis, B., Flasar, M., 2007. C ring fine structures revealed in the thermal infrared. Icarus 191, 691–701.

Altobelli, N., Spilker, L., Leyrat, C., Pilorz, S., 2008. Thermal observations of Saturn's main rings by Cassini CIRS: Phase, emission and solar elevation dependence. Planet. Space Sci. 56, 134–146.

Aumann, H.H., Kieffer, H.H., 1973. Determination of particle sizes in Saturn's rings from their eclipse cooling and heating curves. Astrophys. J. 186, 305–311.

Chandrasekhar, S., 1960. Radiative Transfer. Dover, New York.

Colwell, J.E., Esposito, L.W., Sremčević, M., 2006. Self-gravity wakes in Saturn's A ring measured by stellar occultations from Cassini. Geophys. Res. Lett. 33. L07201.

Colwell, J.E., Esposito, L.W., Sremčević, M., Stewart, G.R., McClintock, W.E., 2007. Self-gravity wakes and radial structure of Saturn's B ring. Icarus 190, 127–144.

Cuzzi, J.N., Lissauer, J.J., Esposito, L.W., Holberg, J.B., Marouf, E.A., Tyler, G.L., Boishot, A., 1984. Saturn's rings: Properties and processes. In: Greenberg, R., Brahic, A. (Eds.), Planetary Rings. Univ. of Arizona Press, Tucson, pp. 73–199.

Cuzzi, J.N., and 10 colleagues, 2002. Saturn's rings: Pre-Cassini status and mission goals. Space Sci. Rev. 104, 209–251.

Dones, L., Cuzzi, J.N., Showalter, M.R., 1993. Voyager photometry of Saturn's A ring. Icarus 105, 184–215.

Esposito, L.W., Lumme, K., 1977. The tilt effect of Saturn's rings. Icarus 31, 157–167.

Esposito, L.W., O'Callaghan, M., Simmons, K.E., Hord, C.W., West, R.A., Lane, A.L., Pomphrey, R.B., Coffeen, D.L., Sato, M., 1983. Voyager photopolarimeter steller occultation of Saturn's rings. J. Geophys. Res. 88, 8643–8649.

Esposito, L.W., and 15 colleagues, 2005. Ultraviolet imaging spectroscopy shows an active saturnian system. Science 307, 1251–1255.

Farinella, P., Vokrouhlický, D., Hartmann, W.K., 1998. Meteorite delivery via Yarkovsky orbital drift. Icarus 132, 378–387.

Ferrari, C., Leyrat, C., 2006. Thermal emission of spherical spinning ring particles: The standard model. Astron. Astrophys. 447, 745–760.

Ferrari, C., Galdemard, P., Lagage, P.O., Pantin, E., Quoirin, C., 2005. Imaging Saturn's rings with CAMIRAS: Thermal inertia of B and C rings. Astron. Astrophys. 441, 379–389.

Flasar, F.M., and 45 colleagues, 2005. Temperatures, winds, and composition in the saturnian system. Science 307, 1247–1251.

French, R.G., Nicholson, P.D., 2000. Saturn's rings. II. Particle sizes inferred from stellar occultation data. Icarus 145, 502–523.
Froidevaux, L., 1981. Saturn's rings: Infrared brightness variation with solar elevation. Icarus 46, 4–17.
Froidevaux, L., Ingersoll, A.P., 1980. Temperatures and optical depths of Saturn's rings and a brightness temperature for Titan. J. Geophys. Res. 85, 5929–5936.
Froidevaux, L., Matthews, K., Neugebauer, G., 1981. Thermal response of Saturn's ring particles during and after eclipse. Icarus 46, 18–26.
Hanel, R., and 15 colleagues, 1981. Infrared observations of the saturnian system from Voyager I. Science 212, 192–200.
Hanel, R., and 12 colleagues, 1982. Infrared observations of the saturnian system from Voyager II. Science 215, 544–548.
Hedman, M.M., Nicholson, P.D., Salo, H., Wallis, B.D., Buratti, B.J., Baines, K.H., Brown, R.H., Clark, R.N., 2007. Self-gravity wake structures in Saturn's A ring revealed by Cassini VIMS. Astron. J. 133, 2624–2629.
Hudgins, D.M., Sanford, S.A., Allamandola, L.J., Tielens, A.G.G.M., 1993. Mid- and far-infrared spectroscopy of ices: Optical constants and integrated absorbances. Astrophys. J. Suppl. 86, 713–870.
Irvine, W.M., Pollack, J.B., 1968. Infrared optical properties of water and ice spheres. Icarus 8, 324–360.
Kawata, Y., 1983. Infrared brightness temperature of Saturn's rings based on the inhomogeneous multilayer assumption. Icarus 56, 453–464.
Kawata, Y., Irvine, W.M., 1975. Thermal emission from a multiple scattering model of Saturn's rings. Icarus 24, 472–482.
Kouchi, A., Greenberg, J.M., Yamamoto, T., Mukai, T., 1992. Extremely low thermal conductivity of amorphous ice: Relevance to comet evolution. Astrophys. J. 388, L73–L76.
Leyrat, C., Ferrari, C., Charnoz, S., Decriem, J., Spilker, L., Pilorz, S., 2008. Spinning particles in Saturn's C ring from mid-infrared observations: Pre-Cassini results. Icarus 196, 625–641.
Lissauer, J.J., Stewart, G.R., 1993. Growth of planets from planetesimals. In: Levy, E.H., Lunine, J.I., Matthews, M.S. (Eds.), Protostars and Planets III. Univ. of Arizona Press, Tucson, pp. 1061–1088.
Lynch, D.K., Mazuk, A.L., Russell, R.W., Hackwell, J.A., Hanner, M.S., 2000. 8- to 13-μm spectra of Saturn's A and B rings. Icarus 146, 43–47.
Marouf, E.A., Tyler, G.L., Zebker, H.A., Simpson, R.A., Eshleman, V.R., 1983. Particle size distributions in Saturn's rings from Voyager 1 radio occultation. Icarus 54, 189–211.
Morishima, R., Salo, H., 2006. Simulations of dense planetary rings IV: Rotating self-gravitating particles with size distribution. Icarus 181, 272–291.
Morrison, D., 1974. Infrared radiometry of the rings of Saturn. Icarus 22, 57–65.
Mullin, T.S., 1984. Glossary. In: Gehrels, T., Matthews, M.S. (Eds.), Saturn. Univ. of Arizona Press, Tucson, pp. 931–945.
Murphy, R.E., 1973. Temperatures of Saturn's rings. Astrophys. J. 181, 87–90.
Murphy, R.E., Cruikshank, D.P., Morrison, D., 1972. Limb darkening of Saturn and thermal properties of the rings from 10 and 20 micron radiometry. Bull. Am. Astron. Soc. 4, 358.
Nicholson, P.D., French, R.G., Campbell, D.B., Margot, J.-L., Nolan, M.C., Black, G.J., Salo, H.J., 2005. Radar imaging of Saturn's rings. Icarus 177, 32–62.
Nolt, I.G., Tokunaga, A., Gillett, F.C., Caldwell, J., 1978. The 22.7 micron brightness of Saturn's rings versus declination of the Sun. Astrophys. J. 219, 63–66.
Nolt, I.G., Barrett, E.W., Caldwell, J., Gillett, F.C., Murphy, R.E., Radostitz, J.V., Tokunaga, A., 1980. IR brightness and eclipse cooling of Saturn's rings. Nature 283, 842–843.
Ohtsuki, K., 1999. Evolution of particle velocity dispersion in a circumplanetary disk due to inelastic collisions and gravitational interactions. Icarus 137, 152–177.
Ohtsuki, K., 2005. Rotation rates of particles in Saturn's rings. Astrophys. J. 626, L61–L64.
Ohtsuki, K., 2006a. Rotation rate and velocity dispersion of planetary ring particles with size distribution. I. Formulation and analytic calculation. Icarus 183, 373–383.
Ohtsuki, K., 2006b. Rotation rate and velocity dispersion of planetary ring particles with size distribution. II. Numerical simulation for gravitating particles. Icarus 183, 384–395.
Ohtsuki, K., Emori, H., 2000. Local N-body simulations for the distribution and evolution of particle velocities in planetary rings. Astron. J. 119, 403–416.
Ohtsuki, K., Toyama, D., 2005. Local N-body simulations for the rotation rates of particles in planetary rings. Astron. J. 130, 1302–1310.
Porco, C.C., and 34 colleagues, 2005. Cassini Imaging Science: Initial results on Saturn's rings and small satellites. Science 307, 1226–1236.
Poulet, F., Cuzzi, J.N., 2002. The composition of Saturn's rings. Icarus 160, 350–358.
Poulet, F., Cruikshank, D.P., Cuzzi, J.N., Roush, T.L., French, R.G., 2003. Composition of Saturn's rings A, B, and C from high resolution near-infrared spectroscopic observations. Astron. Astrophys. 412, 305–316.
Press, W.H., Teukolsky, S.A., Vetterling, W.T., Flannery, B.P., 1986. Numerical Recipes. Cambridge Univ. Press, Cambridge, UK.
Richardson, D.C., 1994. Tree code simulations of planetary rings. Mon. Not. R. Astron. Soc. 269, 493–511.
Rieke, G.H., 1975. Thermal radiation of Saturn and its rings. Icarus 160, 37–44.
Salo, H., 1987. Numerical simulations of collisions between rotating particles. Icarus 70, 37–51.
Salo, H., 1991. Numerical simulations of dense collisional systems. Icarus 90, 254–270.
Salo, H., 1992a. Numerical simulations of dense collisional systems. II. Extended distribution of particle sizes. Icarus 96, 85–106.
Salo, H., 1992b. Gravitational wakes in Saturn's rings. Nature 359, 619–621.
Salo, H., 1995. Simulations of dense planetary rings. III. Self-gravitating identical particles. Icarus 117, 287–312.
Salo, H., Karjalainen, R., 2003. Photometric modeling of Saturn's rings. I. Monte Carlo method and the effect of nonzero volume filling factor. Icarus 164, 428–460.
Salo, H., Schmidt, J., Spahn, F., 2001. Viscous overstability in Saturn's B ring. I. Direct simulations and measurement of transport coefficients. Icarus 153, 295–315.
Salo, H., Karjalainen, R., French, R.G., 2004. Photometric modeling of Saturn's rings. II. Azimuthal asymmetry in reflected and transmitted light. Icarus 170, 70–90.
Schulman, L.M., 2004. The heat capacity of water ice in interstellar or interplanetary conditions. Astron. Astrophys. 416, 187–190.
Sinton, W.M., Macy, W.W., Good, J., Orton, G.S., 1980. Infrared scams of Saturn. Icarus 42, 251–256.
Spilker, L.J., Ferrari, C., Cuzzi, J.N., Showalter, M., Pearl, J., Wallis, B., 2003. Saturn's rings in the thermal infrared. Planet. Space Sci. 51, 929–935.
Spilker, L.J., Pilorz, S.H., Edginton, S.G., Wallis, B.D., Brooks, S.M., Pearl, J.C., Flasar, F.M., 2005. Cassini CIRS observations of a roll-off in Saturn ring spectra at submillimeter wavelengths. Earth Moon Planets 96, 149–163.
Spilker, L.J., and 11 colleagues, 2006. Cassini thermal observations of Saturn's main rings: Implications for particle rotation and vertical mixing. Planet. Space Sci. 54, 1167–1176.
Tokunaga, A.T., Caldwell, J., Nolt, I.G., 1980. The 20-μm brightness temperature of the unilluminated side of Saturn's rings. Nature 287, 212–214.
Vokrouhlický, D., Nesvorný, D., Dones, L., Bottke, W., 2007. Thermal forces on planetary ring particles: Application to the main system of Saturn. Astron. Astrophys. 471, 717–730.
Wisdom, J., Tremaine, S., 1988. Local simulations of planetary rings. Astron. J. 95, 925–940.
Zebker, H.A., Marouf, E.A., Tyler, G.L., 1985. Saturn's rings—Particle size distributions for thin layer model. Icarus 64, 531–548.